



Generalized stacking fault energies and Peierls stresses in refractory body-centered cubic metals from machine learning-based interatomic potentials



Xiaowang Wang ^{a,*}, Shuzhi Xu ^b, Wu-Rong Jian ^b, Xiang-Guo Li ^c, Yanqing Su ^d, Irene J. Beyerlein ^{b,e}

^a Department of Physics, University of California, Santa Barbara, CA 93106-9530, USA

^b Department of Mechanical Engineering, University of California, Santa Barbara, CA 93106-5070, USA

^c Department of Materials Science and Engineering, University of Wisconsin, Madison, WI 53706, USA

^d Department of Mechanical and Aerospace Engineering, Utah State University, Logan, UT 84322-4130, USA

^e Materials Department, University of California, Santa Barbara, CA 93106-5050, USA

ARTICLE INFO

Keywords:

Spectral neighbor analysis potential
Generalized stacking fault energy
Peierls stress
Refractory body-centered cubic metals

ABSTRACT

The generalized stacking fault energies (GSFE) and Peierls stresses are strongly related to the mechanical properties of refractory metals. In this work, the GSFE curves and Peierls stresses of screw and edge dislocations in four body-centered cubic refractory metals (Mo, Nb, Ta, and W) on the {110}, {112}, and {123} slip planes are calculated using molecular statics simulations. A recently developed machine learning (ML)-based interatomic potential, called the spectral neighbor analysis potential (SNAP), is employed in all simulations. The computed GSFE curves achieve reasonable agreement with those from *ab initio* calculations and predict the asymmetry with respect to sense of glide direction on the {112} and {123} planes better than non-ML interatomic potentials. In general, SNAP provides screw dislocation Peierls stresses close to those of density functional theory, closer than those achieved by non-ML potentials. The screw dislocation Peierls stress values confirm slip symmetry on the {110} plane and exhibit pronounced slip asymmetry on the {112} and {123} planes. For all metals, the edge dislocation Peierls stress are the lowest on the {110} plane and the highest on the {112} plane. For screw dislocations, glide on either the {110} or the {123} plane is the easiest.

1. Introduction

Refractory metals are metals with high melting points (above 2200 °C) [1]. This property makes them desirable materials for a wide range of industrial applications [2]. One of the earliest and most well-known of these applications is the use of W in incandescent lighting [3]. Today, refractory metals are present in many cutting-edge technologies as components exposed to extreme environments [4]. Refractory metals, for example, can serve as control rods in nuclear energy reactors [5]. They also find applications in rocket engines, which must sustain the high temperatures from burning rocket fuels. The main engine of Apollo Lunar Modules, for instance, consists of 89% Nb [6].

While the high temperature strength of refractory metals makes them attractive structural materials, it also renders them difficult to shape into useful industrial components [7]. Plastic behavior in metals is realized

by the glide of dislocations on specific crystallographic slip systems or slip modes, and for refractory metals, the stresses required to activate dislocation glide are relatively high compared to traditional metals like steel or aluminum [8]. Dislocation motion involves the breaking and forming of bonds across their crystalline glide planes, roughly similar to shearing the two halves of the crystal across the plane [9]. The potential energy associated with shearing is the generalized stacking fault energy (GSFE) [10], and from GSFE calculations, a measure of the ideal shear strength can be obtained for the plane [11]. Another basic measure of dislocation glide resistance is the Peierls stress, the minimum resolved shear stress required for an isolated, stationary dislocation to first move [12]. In some cases, the GSFE and Peierls stress can be related [13]. A study on body-centered cubic (BCC) Fe demonstrated how variations in the GSFE affected the core structure of the edge character dislocations [14].

* Corresponding author.

E-mail address: xiaowangwang@ucsb.edu (X. Wang).

Table 1

Lattice parameters a_0 (in Å) and equilibrium bulk energy per atom E_{bulk} (in eV). Volume-energy measurement-based DFT results are from Ref. [16]. All other results are newly calculated in this work, but closely following Ref. [16].

| Measurement | Method | Mo | | Nb | | Ta | | W | |
|---------------|--------|-------|-------------------|-------|-------------------|-------|-------------------|-------|-------------------|
| | | a_0 | E_{bulk} | a_0 | E_{bulk} | a_0 | E_{bulk} | a_0 | E_{bulk} |
| Relaxation | SNAP | 3.167 | -10.85 | 3.326 | -10.1 | 3.317 | -11.85 | 3.181 | -12.97 |
| Relaxation | DFT | 3.162 | -10.92 | 3.322 | -10.09 | 3.321 | -11.81 | 3.184 | -12.95 |
| Volume-energy | SNAP | 3.168 | -10.85 | 3.326 | -10.1 | 3.32 | -11.85 | 3.181 | -12.97 |
| Volume-energy | DFT | 3.16 | -10.92 | 3.324 | -10.09 | 3.32 | -11.81 | 3.184 | -12.95 |

Plastic deformation in refractory metals may possibly occur by multiple distinct slip planes, commonly the {110}, {112}, and {123} planes [15]. To date, studies on Peierls stresses of refractory metals often focused on the {110} plane and less so on the {112} or {123} plane. Obtaining key insights into the deformation behavior refractory metal components would benefit from a comprehensive understanding of how these critical energies and stresses vary with crystallographic glide plane and dislocation character.

Common methods for characterizing dislocation structures and their behavior are atomic-scale simulation methods, such as density functional theory (DFT) and molecular statics (MS) and dynamics (MD) calculations. DFT is the most accurate of the three methods and has been used in a few studies to calculate GSFE curves in the {111} direction on the {110} plane and, in few cases, the {112} or {123} plane, for six refractory BCC metals: Cr [16], Mo [17,16], Nb [18,19,16], Ta [20,16], V [21,16], and W [22–26,16]. Peierls stress calculations via DFT for the {110} and/or {112} planes have also been carried out for all these metals: Cr [27], Mo [28–32], Nb [31,33], Ta [29,34,31,33], V [31,33], and W [22,31,33,32]. DFT calculations are usually limited to a relatively small number of atoms, in the range of 20–200 atoms. MS or MD simulations, on the other hand, can be used to study dislocation behavior in model crystals of much larger size scales [35], although with less accuracy due to the reliance on interatomic potentials [36,34]. In this regard, many of the commonly used interatomic potentials, such as the embedded-atom method (EAM) and the Finnis–Sinclair (F-S) potentials, have been found to have a few issues [37,38]. Classical interatomic potentials have been shown to perform poorly in calculating Peierls stresses in BCC metals, producing values more than 100% greater than DFT calculations due to omission of quantum effects [39]. For BCC Fe, properties, such as energies of defective configurations, Peierls potentials associated with screw dislocations, and other fundamental bulk properties are not satisfactorily reproduced by EAM and F-S potentials [40].

Recently, machine learning (ML)-based interatomic potentials have emerged as a new class of potentials and are rapidly gaining popularity [41]. Similar to classical interatomic potentials, ML potentials incorporate quantum effects only in the construction of the potential. However, ML potentials attempt to remedy the loss of accuracy through optimization of potential function parameters through an ML algorithm [42]. Unlike classical interatomic potentials, physical approximations are not used other than in the reference electronic structure during its

construction stage. ML potentials have achieved near-DFT accuracy in calculating material properties with computational cost more than one order of magnitude lower than DFT [43]. In addition, unlike DFT in which the computational cost scales quadratically or cubically with the number of atoms, the computational cost of atomistic simulations with short-range interatomic potentials scales linearly with the number of atoms [44].

Several kinds of ML potentials have been used for atomistic simulations [45], including the high-dimensional neural network potential (NNP), spectral neighbor analysis potential (SNAP), Gaussian approximation potential (GAP), and moment tensor potential (MTP). They differ in accuracy, computational cost, and training difficulty. In developing an ML potential for a new material, training sets that span a wide variety of conditions are used to allow the potential to learn and improve through ML algorithm. An effective ML algorithm means less training difficulty in that less training simulations need to be performed for the potential to achieve a certain accuracy. Under these criteria, the most accurate ML potentials are the GAP and MTP potentials. However, SNAP exceeds GAP in having lower computational cost and exceeds MTP in having higher extrapolability [46]. In addition, SNAP has been shown to reach reasonable accuracy, while requiring less training data when fitting a new material [47]. Note that SNAP is about two to three orders of magnitude higher in computational cost than EAM [48].

In this paper, we use atomistic simulations employing the SNAP ML potential [49] to calculate the GSFE curves and Peierls stresses for edge and screw dislocations on three {110}, {112}, and {123} planes in Mo, Nb, Ta, and W. We demonstrate that on all three planes, the GSFE curves from SNAP agree well with those from DFT. We show that the group VI metals, Mo and W, achieve higher peak energies in the GSFE curves compared to the group V metals, Nb and Ta. In addition, we show that for edge dislocations, the Peierls stress are the lowest on the {110} plane and the highest on the {112} plane. For screw dislocations, however, glide on either the {110} or {123} plane is the easiest. Our results confirm the twinning/anti-twinning slip asymmetry in screw dislocation Peierls stress in the {112} plane. We reveal that like the {112} plane, the highest order {123} plane also exhibits glide asymmetry. The differences in screw-to-edge Peierls stress ratio and slip-plane anisotropy among these four metals are also discussed.

2. Basic structural parameters

We first validate SNAP against DFT by calculating the lattice parameter a_0 and three elastic constants (C_{11} , C_{12} , C_{44}) associated with each BCC metal. For a_0 , two independent calculations are conducted. The first measurement is based on relaxation, in which a BCC unit cell with a pre-defined lattice parameter $a_0^\dagger = 3.2 \text{ \AA}$ is built and the system is relaxed such that the three normal stress components are zero. a_0 is obtained from the resultant unit cell volume. The second calculation is based on the volume-energy relation, which involves constructing a series of periodic simulation cells of different a_0^\dagger . The bulk energy per atom, E_{bulk}^\dagger , is computed for each cell and a_0 is obtained from the cell with the lowest energy per atom, E_{bulk} [50]. Results are shown in Fig. A.1.

Table 2

Elastic constants C_{11} , C_{12} , and C_{44} (in GPa). The isotropic shear modulus in Hill form, μ , is calculated based on C_{11} , C_{12} , and C_{44} . DFT results are from Ref. [16].

| | Method | Mo | Nb | Ta | W |
|----------|--------|--------|--------|--------|--------|
| C_{11} | SNAP | 434.85 | 266.09 | 256.79 | 560.28 |
| | DFT | 467.85 | 249.01 | 268.13 | 520.35 |
| C_{12} | SNAP | 169.16 | 142.57 | 160.86 | 217.81 |
| | DFT | 158.75 | 135.43 | 160.35 | 199.88 |
| C_{44} | SNAP | 95.87 | 20.3 | 66.21 | 154.64 |
| | DFT | 100.22 | 18.1 | 77.38 | 142.42 |
| μ | SNAP | 109.27 | 32.32 | 58.19 | 161.08 |
| | DFT | 119.29 | 29.23 | 66.94 | 149.3 |

Table 3

Number of atoms and number of atomic planes along the y direction for each plane.

| Plane | No. of atoms | No. of planes |
|-------|--------------|---------------|
| {110} | 72 | 12 |
| {112} | 72 | 24 |
| {123} | 84 | 28 |

The list of results in [Table 1](#) demonstrates that for the same metals, (i) with the same method, the two measurements of a_0 and E_{bulk} are very close and (ii) for the same measurement, SNAP agrees well with DFT. In the remainder of this paper, values of a_0 based on the volume-energy measurement will be used.

Values of C_{11} , C_{12} , and C_{44} are obtained using the stress-strain method [\[51\]](#). The SNAP elastic constants also achieve good agreement with the DFT constants, differing by less than 10%, as shown in [Table 2](#). Based on these results, we proceed with confidence to use SNAP to calculate the GSFE and Peierls stresses for these four refractory metals. LAMMPS [\[52\]](#) is used for all MS simulations in this paper.

3. Generalized stacking fault energy

3.1. Methodology

With SNAP, we calculate GSFE curves using a method similar to that

used in Ref. [\[51\]](#). Simulation cells are first constructed with a 12 Å vacuum on one end in the y direction to prevent periodic images from interacting with each other. BCC crystal lattice structures are then created inside the simulation cells (except the vacuum region). For each metal, three different lattice orientations are adopted by making the x - z plane correspond to the glide plane of interest. For the {110} plane calculation, the orientation of the crystal is set to be $x\langle 112 \rangle$, $y\langle 110 \rangle$, $z\langle 111 \rangle$. Likewise, for the {112} plane, the model orientation is $x\langle 110 \rangle$, $y\langle 112 \rangle$, and $z\langle 111 \rangle$. Finally, for the {123} plane, the crystallographic orientation is $x\langle 145 \rangle$, $y\langle 123 \rangle$, and $z\langle 111 \rangle$.

Each GSFE curve is computed by displacing the top half layers of atoms with respect to the bottom half in the $z\langle 111 \rangle$ direction. Displacements are made as equal increment, with each increment being a fraction of 0.025 of the Burgers vector magnitude. Following each displacement, the top and bottom atomic layers are held fixed, while the remaining layers are allowed to relax only in the y direction. Relaxation through energy minimization is achieved via the conjugate gradient scheme. The minimization process is terminated when (i) the quotient of the change in energy in successive iterations and the most recent energy magnitude is less than 10^{-12} or (ii) when the global force vector length of all atoms is less than or equal to 10^{-12} eV/Å. It follows that 41 GSFE values are obtained along each curve.

In GSFE calculations, once the displacement is set, the atoms are not relaxed along the x direction during energy minimization. The effects of relaxing atoms along the x direction are studied in Mo and Nb. Results, presented in [Fig. B.2](#), show that this relaxation leads to little changes in

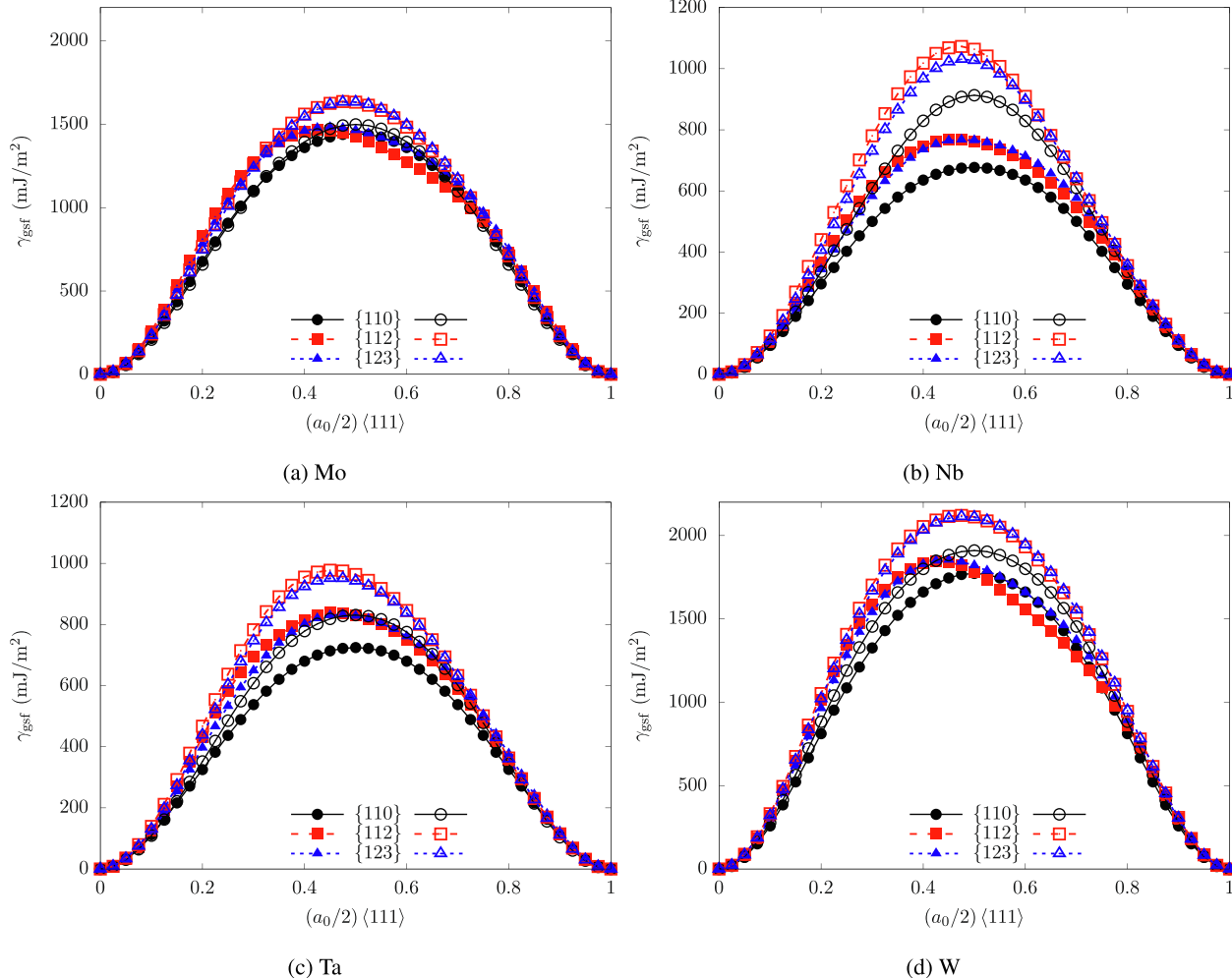


Fig. 1. Relaxed GSFE curves on the three planes in four BCC refractory metals. SNAP-based results (open symbols) are compared with those from previous DFT calculations (filled symbols) from Ref. [\[16\]](#).

Table 4

USFEs γ_{usf} (in mJ/m^2) and ideal shear strengths T_{is} (in GPa). DFT results are from Ref. [16]. EAM potentials for Mo, Ta, and W are from Ref. [54], and that for Nb is from Ref. [55]. Note that EAM results for Mo and Nb have been reported in terms of γ_{usf} [51] and T_{is} [60].

| Plane | Method | Mo | Nb | Ta | W |
|-------|-----------------------|---------|--------|--------|---------|
| {110} | γ_{usf} | SNAP | 1498.8 | 912.94 | 830.8 |
| | DFT | 1443.39 | 676.78 | 724.46 | 1772.74 |
| | EAM | 1458.05 | 604.87 | 751.11 | 1740.14 |
| | T_{is} | SNAP | 17.41 | 9.64 | 9.32 |
| | DFT | 17.7 | 7.51 | 7.78 | 20.99 |
| | EAM | 33.1 | 14.1 | 8.74 | 15.56 |
| {112} | γ_{usf} | SNAP | 1635.8 | 1072.7 | 977.64 |
| | DFT | 1465.13 | 768.82 | 838.39 | 1845.83 |
| | EAM | 1689.03 | 697.23 | 868.3 | 2011.13 |
| | T_{is} | SNAP | 20.2 | 12.27 | 12.21 |
| | DFT | 21.67 | 9.88 | 11.4 | 26.46 |
| | EAM | 58.4 | 24.5 | 10.14 | 18.44 |
| {123} | γ_{usf} | SNAP | 1632.7 | 1031 | 950.93 |
| | DFT | 1481.35 | 767.42 | 832.34 | 1854.3 |
| | EAM | 1657.93 | 684.71 | 852.26 | 1975.71 |
| | T_{is} | SNAP | 19.75 | 11.59 | 11.65 |
| | DFT | 20.35 | 8.91 | 9.97 | 24.99 |
| | EAM | 19.3 | 8.1 | 9.94 | 8.11 |

GSFE.

A prior DFT study in face-centered cubic (FCC) Ir and Rh [53] found that the calculated GSFEs can be overestimated if the number of atomic planes used in the simulation cell is too small. Hence, we study the effect of the number of atomic planes on GSFE curves, as shown in Fig. C.3. The study is done in Nb, whose cutoff distance, 4.701 Å, is larger than those of the other three metals, i.e., 4.6 Å for Mo, 4.499 Å for Ta, and 4.499 Å for W. It is found that, when the number is too small, the GSFE is overestimated, similar to Ir and Rh. More importantly, the analysis confirmed that the numbers of atomic planes used in the present calculations (summarized in Table 3) provide converged GSFE values.

For the comparisons between SNAP and DFT that follow, we focus on key properties of the GSFE curves, including the unstable stacking fault energy (USFE) γ_{usf} and the ideal shear strength T_{is} . They can be calculated from the GSFE curves γ_{gsf} via [11]:

$$\gamma_{\text{usf}} = \max[\gamma_{\text{gsf}}(d_z)] \quad (1)$$

$$T_{\text{is}} = \max \left[\frac{\partial \gamma_{\text{gsf}}(d_z)}{\partial d_z} \right] \quad (2)$$

Since γ_{usf} and T_{is} are obtained based on discrete GSFE values, one may wonder whether the number of GSFE values, currently 41, is sufficient. To test this, we recalculated the GSFE curves on the three slip planes in Ta and W with 101 values along each curve, and recalculated γ_{usf} and T_{is} . Results, shown in Table D.1, suggest that 41 GSFE values along each curve are sufficient.

In addition to the GSFE curves, we also calculate the entire GSFE surfaces on the three slip planes in the four metals. The model and method are the same, except that the top half atomic layers are also displaced along the x direction, in addition to the z direction, to generate the entire energetic surface. Note that DFT calculations to date have only computed the GSFE curves in the $\langle 111 \rangle$ slip direction [16], not the entire GSFE surfaces for any plane.

3.2. Results and discussion

Fig. 1 presents the calculated GSFE curves for all three planes in all

four metals. The MS calculation with SNAP generally produces higher GSFE compared to DFT. The GSFE curves for Mo achieve the best agreement with DFT, especially for the $\{110\}$ plane, which only shows a 4% discrepancy in the peak value, the γ_{usf} . The results for Nb display the poorest agreement with DFT, where the largest discrepancy of 39% in the γ_{usf} is seen for the $\{112\}$ plane.

According to the hard-sphere model for the BCC lattice, the peak γ_{usf} in the $\{110\} \langle 111 \rangle$ GSFE curve should occur at a displacement of $b/2 = (a_0/4)\langle 111 \rangle$, indicating that the $\{110\}$ GSFE curve is symmetric [9]. In agreement, calculations from both SNAP and DFT on the $\{110\}$ planes exhibit symmetry for all four metals. By the same hard-sphere model, the displacement at γ_{usf} should be $b/3$ for the $\{112\}$ and $\{123\}$ higher order planes, making their GSFE curves asymmetric. While the DFT calculated curves exhibit this asymmetry, the SNAP calculated GSFE curves show a slightly lower degree of asymmetry. The closest result to DFT is realized with Ta, and the farthest one with W. Nonetheless, the prediction of asymmetry made by SNAP is an improvement from those provided by previous non-ML potentials. For instance, the calculated GSFE curves on the $\{112\}$ and $\{123\}$ planes of W with an EAM or an F-S potential are symmetric [25]. Although interatomic potentials include quantum effects in their construction, simulations with these potentials do not capture their effect on atomic arrangements. The fact that interatomic potentials show less or no degree of asymmetry could suggest that in order for the GSFE curves to exhibit asymmetry as seen in DFT, quantum effects need to be taken into account in the calculations as well.

The γ_{usf} and T_{is} are compared in Table 4. Unlike γ_{usf} , T_{is} from SNAP lies within $\pm 10\%$ from that of DFT. Table 4 also compares the SNAP and DFT results with those from EAM potentials (Mo [54], Nb [55], Ta [54], W [54]). In γ_{usf} , the EAM results are slightly closer to DFT than SNAP; however, in T_{is} , SNAP results are clearly in most cases closer to DFT.

Results in Table 4 show that the group VI metals, Mo and W, have higher γ_{usf} and T_{is} than the group V metals, Nb and Ta. For the same plane, the metal with the highest γ_{usf} among the four metals is W, with a value approximately twice that of Ta, which has the lowest γ_{usf} , another feature in which SNAP and DFT agree.

Besides the GSFE curves, the entire GSFE surfaces in Ta and W are presented in Fig. 2 as references. The GSFE surfaces in Mo and Nb, which are not shown, are similar. It is found that the GSFE surfaces on different planes differ greatly from each other, and from that in FCC metals [53]. Notably, on all three planes in all four BCC metals, all $\langle 111 \rangle$ GSFE curves sit at local minima, suggesting that the full dislocations would not be associated into partials as in FCC metals [56–59]. This also explains why allowing relaxation along the x direction does not alter the GSFE curve values (Fig. B.2).

4. Peierls stress

4.1. Methodology

We employ the periodic array of dislocations (PAD) model to calculate the Peierls stress [61]. Table 5 specifies the number of atoms, crystallographic orientations, and initial simulation cell edge lengths (L_x , L_y , L_z) of the simulation models. An edge or a screw dislocation with Burgers vector magnitude of $b = (a_0/2)\langle 111 \rangle$ is inserted into the center of the simulation cell by displacing atoms following linear elasticity theory [62–64]. The dislocation line is aligned with the z axis and the $x-z$ plane corresponds to the slip plane, in which the dislocation lies. Periodic boundary conditions are applied in the x and z directions and traction-free boundary conditions are in the y direction [65]. Fig. 3 shows the core structures of six dislocations in Nb.

An incremental strain tensor ϵ is applied by gradually applying a

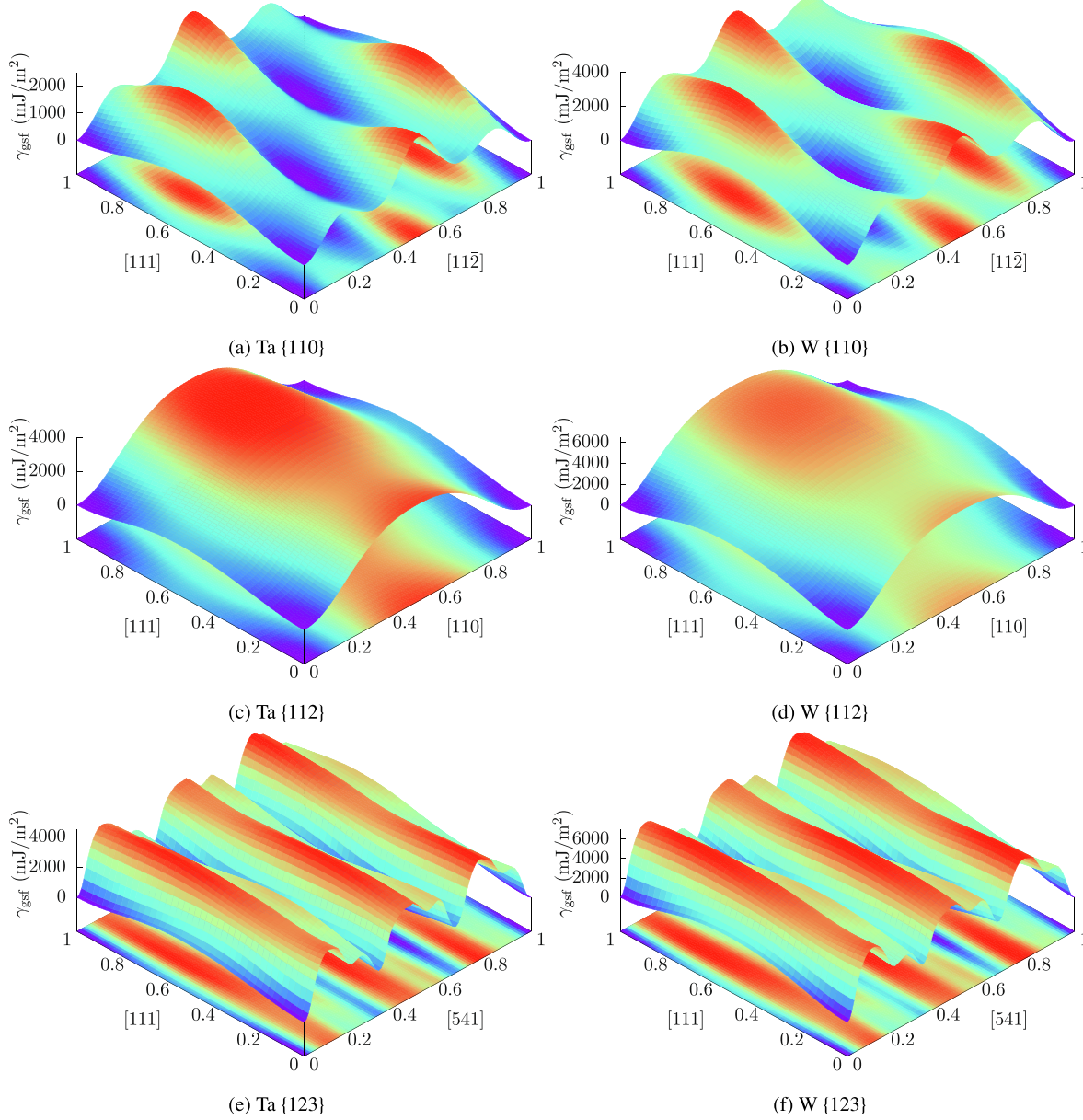


Fig. 2. Relaxed GSFE surfaces on {110}, {112}, and {123} planes in Ta and W, based on SNAP.

Table 5

The number of atoms, crystallographic orientations, and edge lengths for each simulation cell for Nb. The cells of other metals are the same in terms of number of atoms and crystallographic orientations, but the edge lengths are scaled with respect to their own lattice parameters.

| Plane | Dislocation | No. of atoms | x | y | z | L_x (Å) | L_y (Å) | L_z (Å) |
|-------|-------------|--------------|-----------------|-----------------|-----------------|-----------|-----------|-----------|
| {110} | Edge | 70308 | [111] | [1 $\bar{1}$ 0] | [11 $\bar{2}$] | 401.8 | 395.1 | 8.1 |
| | Screw | 49980 | [$\bar{1}$ 12] | [1 $\bar{1}$ 0] | [111] | 399.2 | 399.8 | 5.8 |
| {112} | Edge | 80352 | [111] | [$\bar{1}$ 12] | [11 $\bar{0}$] | 401.8 | 391.1 | 9.4 |
| | Screw | 49980 | [$\bar{1}$ 10] | [$\bar{1}$ 12] | [111] | 399.8 | 399.2 | 5.8 |
| {123} | Edge | 187488 | [111] | [$\bar{1}$ 23] | [54 $\bar{1}$] | 401.8 | 398.2 | 21.6 |
| | Screw | 51072 | [$\bar{5}$ 41] | [$\bar{1}$ 23] | [111] | 409.5 | 398.2 | 5.8 |

simple shear to the simulation cell. Each simulation cell starts as a cuboid and distorts to a triclinic shape with an increasing shear strain. The non-zero shear strain component for the screw dislocation case is ϵ_{yz} , while the non-zero component for the edge dislocation case is ϵ_{xy} . All other strain components are zero. The strain increment at each step is

2×10^{-5} for edge dislocations and 2×10^{-6} for screw dislocations, until the maximum strain of 0.12 is reached. Similar increments were used in a recent MS work for edge and screw dislocations in Mo and Nb [60,68] and an earlier MS work for an edge dislocation in Fe [61]. With SNAP, we have recalculated selected Peierls stresses with smaller stress

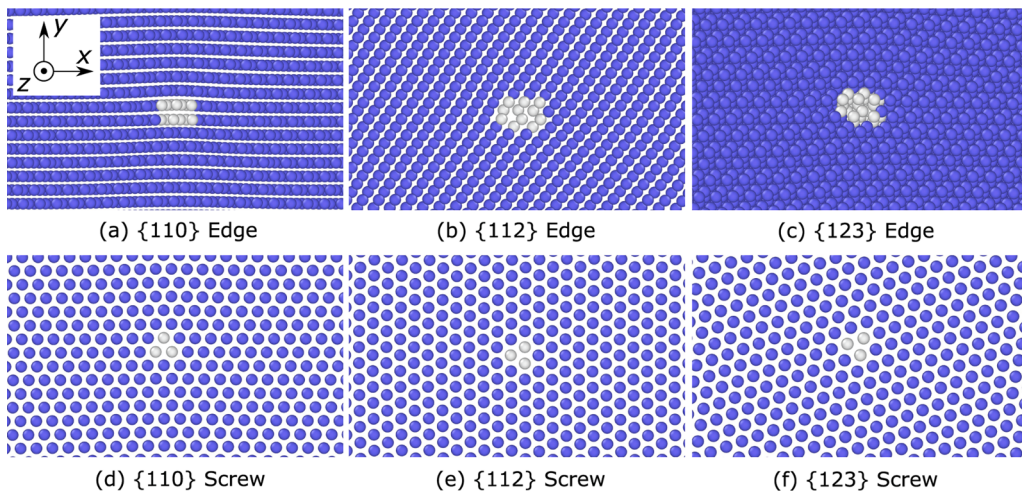


Fig. 3. Atomistic structures of six dislocation cores in Nb, visualized in OVITO [66]. Atoms are colored by adaptive common neighbor analysis [67]: blue and white correspond to BCC and disordered local lattice structures, respectively.

increments and found the results to differ by less than 1%.

Following each incremental strain, two minimization procedures are employed: the conjugate gradient algorithm and the fast inertial relaxation engine method [69]. The minimization stops when either of the conditions stated earlier in the GSFE calculations in Section 3.1 is met. The Peierls stress is then identified as the minimum stress at which the dislocation starts to move. In all planes, we carry out separate simulations for shearing in the positive and negative directions to assess the slip asymmetry in the Peierls stress. We refer to positive shearing as “forward”, and negative shearing as “backward”. For the {112} plane only, the backward sense we assigned is commonly known as the anti-twinning direction, while the forward one the twinning direction [70].

Before embarking on systematic atomistic simulations in the four refractory metals, we conduct a study on the effects of the simulation cell size on the Peierls stress value. For this, we choose Nb with an edge dislocation on the {112} plane and apply the shear strain in the twinning direction. For the effect of dislocation line length, L_x and L_y are fixed, while L_z is varied from 4.7, 9.4, 14.1, to 18.8 Å. For the effect of the other

two edge lengths, a fixed dislocation line length ($L_z = 9.4$ Å) is chosen, while $L_x \times L_y$ is varied from 301.0×293.3 Å², 401.8×391.1 Å², to 502.6×488.8 Å². It is shown that in general the Peierls stress increases as L_z decreases or as L_x and L_y increase. Note that a recent study on the same dislocation in Nb using an EAM potential [55] or an F-S potential [71] showed that the effect of L_x and L_y on the Peierls stress value depends on the interatomic potential [68], hence justifying the need to identify these dimensions for SNAP. Overall, the resulting Peierls stresses here do not show a strong correlation with the simulation cell size. With changing L_z , the Peierls stress varies within ±2%, and with varying L_x and L_y , it varies within ±8%. In all subsequent simulations, we employ the simulation cell sizes given in Table 5 for Nb; cell sizes are scaled with lattice parameters for the other three metals.

4.2. Results and discussion

In this section, the MS results using SNAP are compared with those from previous MS simulations, near 0 K MD simulations, *ab initio*

Table 6

Peierls stress values (in MPa) for edge dislocations on different slip planes in four BCC metals. All used MS simulations except [73], which used near 0 K MD simulations. Data from Ref. [68] were taken for comparable sizes (edge length or diameter per dislocation ≈ 50 nm) and the same shear-controlled loading as the present work. T: twinning; AT: anti-twinning; fw: forward; bw: backward.

| Metal | Model | Potential | {110} _{fw} | {110} _{bw} | {112} _{fw} (T) | {112} _{bw} (AT) | {123} _{fw} | {123} _{bw} |
|---------|------------|-----------|---------------------|---------------------|-------------------------|--------------------------|---------------------|---------------------|
| Mo | PAD | SNAP [73] | 138 | 134 | 1037 | 710 | 231 | 208 |
| Mo [73] | FBC | SNAP [73] | 76 | — | — | — | — | — |
| Mo [60] | PAD | EAM [54] | 50 | 50 | 533 | 734 | 160 | 117 |
| Mo [74] | FBC | MEAM [74] | — | — | 150 | — | — | — |
| Nb | PAD | SNAP [73] | 23 | 25 | 282 | 316 | 31 | 85 |
| Nb [73] | FBC | SNAP [73] | 29 | — | — | — | — | — |
| Nb [60] | PAD | EAM [55] | 6 | 6 | 118 | 99 | 12 | 13 |
| Nb [68] | FBC | EAM [71] | — | — | 509 | 577 | — | — |
| Nb [68] | FBS | EAM [71] | — | — | 493 | 574 | — | — |
| Nb [68] | PAD | EAM [71] | — | — | 504 | 549 | — | — |
| Nb [68] | Dipole-H | EAM [71] | — | — | 517 | 567 | — | — |
| Nb [68] | Dipole-V | EAM [71] | — | — | 516 | 567 | — | — |
| Nb [68] | Quadrupole | EAM [71] | — | — | 524 | 566 | — | — |
| Nb [68] | FBC | EAM [55] | — | — | 97 | 121 | — | — |
| Nb [68] | FBS | EAM [55] | — | — | 102 | 129 | — | — |
| Nb [68] | PAD | EAM [55] | — | — | 105 | 94 | — | — |
| Nb [68] | Dipole-V | EAM [55] | — | — | 119 | 99 | — | — |
| Nb [68] | Quadrupole | EAM [55] | — | — | 121 | 101 | — | — |
| Ta | PAD | SNAP [73] | 20 | 21 | 162 | 172 | 4 | 4 |
| Ta [73] | FBC | SNAP [73] | 41 | — | — | — | — | — |
| Ta [75] | FBS | F-S [71] | 30 | — | — | — | — | — |
| W | PAD | SNAP [73] | 8 | 7 | 2276 | 1042 | 736 | 213 |
| W [73] | FBC | SNAP [73] | 56 | — | — | — | — | — |

Table 7

Peierls stress or CRSS (in MPa) for screw dislocations on different slip planes in Mo.

| Method | Model | Potential | $\{110\}_{fw}$ | $\{110\}_{bw}$ | $\{112\}_{fw}$ (T) | $\{112\}_{bw}$ (AT) | $\{123\}_{fw}$ | $\{123\}_{bw}$ |
|----------|------------|-----------|----------------|----------------|--------------------|---------------------|----------------|----------------|
| MS | PAD | SNAP [73] | 4054 | 4054 | 4317* | 5510* | 3932* | 4808* |
| MS [76] | Quadrupole | F-S [71] | 2400 | — | — | — | — | — |
| MS [60] | PAD | EAM [54] | — | — | 2496 | 3842 | — | — |
| MS [74] | FBC | MEAM [74] | 1790 | — | 2020 | 2360 | — | — |
| MS [77] | FBC | BOP [77] | 2600 | — | 2800 | 3500 | — | — |
| MS [78] | GFBC | MGPT [78] | 866 | — | 1235 | 1876 | — | — |
| MS [79] | GFBC | MGPT [80] | 2610 | — | 2340 | 7290 | — | — |
| MS [81] | FBS | MGPT [80] | — | — | 3440* | — | — | — |
| MS [82] | FBS | MGPT [80] | 6192 | — | 3440* | — | — | — |
| MS [78] | FBC | F-S [71] | 2354 | — | 2372 | 4199 | — | — |
| MS [83] | FBS | F-S [71] | 3510 | — | 3510 | 5990 | — | — |
| MD [73] | FBC | SNAP [73] | 1376 | — | — | — | — | — |
| TB [76] | Quadrupole | EDTB [84] | 3800 | — | — | — | — | — |
| DFT [30] | Quadrupole | USPP [85] | 1800 | — | — | — | — | — |
| DFT [28] | GFBC | USPP [85] | 2085 | — | 1740 | 3480 | — | — |
| DFT [32] | Quadrupole | USPP [85] | 1350 | — | — | — | — | — |
| DFT [31] | Quadrupole | PAW [86] | 1600 | — | — | — | — | — |
| DFT [29] | GFBC | USPP [85] | 2420 | — | 1738 | 3173 | — | — |
| Exp [87] | | | 870 | — | 690 | — | — | — |
| Exp [88] | | | 730 | — | — | — | — | — |

calculations, and experiments. We exclude estimates of Peierls stress calculated from the GSFE, e.g., Ref. [72,13]. The number of different potentials used previously is large, including the F-S, EAM, modified embedded-atom method (MEAM), bond-order potential (BOP), modified generalized pseudo potential theory (MGPT), first-principles-based embedded atom model force field (qEAM-FF), and the angular dependent potential (ADP). The *ab initio* calculations used are either DFT or the tight-binding (TB) method. The TB calculations used the environment-dependent tight-binding (EDTB) potential, while the DFT calculations employed the projector augmented wave (PAW) method, ultrasoft pseudopotential (USPP), and norm-conserving pseudopotential (NCPP).

In addition to the interatomic potential, prior MD and MS works used different initial dislocation configurations for calculating the Peierls stress. As mentioned, for most of the SNAP Peierls stress calculations here, we use the PAD configuration. Apart from PAD, six other model configurations have been adopted in the literature, namely the fixed boundary circle (FBC), fixed boundary square (FBS), horizontal dipole (dipole-H), vertical dipole (dipole-V), quadrupole, and Green's function boundary condition (GFBC) models. In a recent study, the Peierls stresses for an edge dislocation on the {112} plane in Nb calculated using PAD and the first five aforementioned models were compared [68]. It was found that even with the same interatomic potential, cell size, material, and dislocation character, these six configurations produce significantly different Peierls stresses. In addition, only the Peierls stress from the PAD model converged to a single value as the simulation cell increased. In this work, at the end of the discussion, for the screw dislocation in Ta and W, we compare the SNAP Peierls stress from six model configurations.

4.2.1. Peierls stress of edge dislocations

Table 6 summarizes the calculated Peierls stresses for edge dislocations. In all cases, the dislocation glides on the habit plane. For comparison, Table 6 also lists edge dislocation Peierls stresses previously calculated with atomistic simulations, involving other interatomic potentials and/or other model configurations. To the best of our knowledge, neither *ab initio* calculations nor measured values for the Peierls stresses of edge dislocations in any of these metals have been previously reported.

Considering all Peierls stresses computed to date shows substantial variation among them. Li et al. [73] used the same SNAP to calculate the Peierls stresses on the {110} plane in all four metals but in near 0 K MD simulations. For Nb and Ta, their values are close to ours, within 20 MPa, but for Mo and W, there exist larger differences. In general, discrepancies can be attributed to the choice of cell size and model configuration. They used the FBC model configuration and a smaller cell size of 20 nm diameter compared to the approximately 40 nm size used in the current PAD configuration. The remaining prior atomistic simulation studies used the MS method with non-ML interatomic potentials. For all three planes in Nb and Mo, the SNAP results are higher by approximately 93% than the Peierls stresses recently calculated using EAM potentials [60]. The Peierls stress on the {112} plane calculated for Mo using an MEAM potential [74] is much smaller, by 89% compared to the value of this study. Jian et al. [68] computed Peierls stresses of Nb in both twinning and anti-twinning directions on the {112} plane using an EAM [55] and an F-S potential [71]. Using the same loading mode, model configuration, and a similar cell size as here, their results when using EAM are higher by 330% than ours but when using F-S, they are lower than ours. In Ta, another calculation on the {110} plane using an

Table 8

Peierls stress or CRSS (in MPa) of screw dislocations on different slip planes in Nb.

| Method | Model | Potential | $\{110\}_{fw}$ | $\{110\}_{bw}$ | $\{112\}_{fw}$ (T) | $\{112\}_{bw}$ (AT) | $\{123\}_{fw}$ | $\{123\}_{bw}$ |
|----------|------------|-----------|----------------|----------------|--------------------|---------------------|----------------|----------------|
| MS | PAD | SNAP [73] | 840 | 827* | 1452* | 2106* | 1177* | 568* |
| MS [90] | FBC | EAM [90] | 1313* | — | 1130 | 3844 | — | — |
| MS [60] | PAD | EAM [55] | — | — | 859 | — | — | — |
| MS [68] | FBC | EAM [90] | — | — | 1264 | — | — | — |
| MD [73] | FBC | SNAP [73] | 889 | — | — | — | — | — |
| DFT [31] | Quadrupole | PAW [86] | 740 | — | — | — | — | — |
| DFT [33] | Quadrupole | USPP [85] | 650–860 | — | — | — | — | — |
| Exp [91] | | | 415 | — | — | — | — | — |

Table 9

Peierls stress or CRSS (in MPa) of screw dislocations on different slip planes in Ta.

| Method | Model | Potential | $\{110\}_{fw}$ | $\{110\}_{bw}$ | $\{112\}_{fw}$ (T) | $\{112\}_{bw}$ (AT) | $\{123\}_{fw}$ | $\{123\}_{bw}$ |
|-----------|------------|--------------|----------------|----------------|--------------------|---------------------|----------------|----------------|
| MS | PAD | SNAP [73] | 956* | 956* | 893* | 3583* | 845* | 2123* |
| MS [75] | FBS | F-S [71] | 2785 | — | — | — | — | — |
| MS [92] | FBC | qeAM-FF [93] | 740 | — | — | — | — | — |
| MS [83] | FBS | F-S [71] | 5916 | — | 4120 | 14832 | — | — |
| MS [78] | FBC | F-S [71] | 3060* | — | 2149 | — | — | — |
| MS [82] | FBS | MGPT [20] | 1875 | — | 1375* | — | — | — |
| MS [20] | GFBC | MGPT [20] | 640* | — | 605 | 1400 | — | — |
| MS [89] | FBS | F-S [71] | 2864* | — | 2033 | 7207 | — | — |
| MS [89] | FBS | EAM [94] | 2023 | — | 2320 | 8624* | — | — |
| MS [89] | FBS | EAM [95] | 5698* | — | 3634 | 9416 | — | — |
| MS [89] | FBS | EAM [96] | 3357* | — | 2012 | 8357* | — | — |
| MS [89] | FBS | ADP [97] | 1242* | — | 842 | 4086* | — | — |
| MD [73] | FBC | SNAP [73] | 912 | — | — | — | — | — |
| MD [98] | Dipole-H | qeAM-FF [93] | 1800 | — | — | — | — | — |
| MD [99] | Dipole-H | qeAM-FF [93] | — | — | 790 | 1430 | — | — |
| MD [34] | Quadrupole | qeAM-FF [93] | 655 | — | 575 | 1075 | — | — |
| DFT [34] | Quadrupole | NCPP [100] | 1410–1760 | — | — | — | — | — |
| DFT [29] | GFBC | USPP [85] | 1550 | — | 701 | 3591 | — | — |
| DFT [31] | Quadrupole | PAW [86] | 860 | — | — | — | — | — |
| DFT [33] | Quadrupole | USPP [85] | 810–920 | — | — | — | — | — |
| Exp [101] | | | 340 | — | — | — | — | — |

Table 10

Peierls stress or CRSS (in MPa) of screw dislocations on different slip planes in W.

| Method | Model | Potential | $\{110\}_{fw}$ | $\{110\}_{bw}$ | $\{112\}_{fw}$ (T) | $\{112\}_{bw}$ (AT) | $\{123\}_{fw}$ | $\{123\}_{bw}$ |
|-----------|------------|-----------|----------------|----------------|--------------------|---------------------|----------------|----------------|
| MS | PAD | SNAP [73] | 3773 | 3772 | 3958* | 5937 | 3689 | 4569* |
| MD [73] | FBC | SNAP [73] | 1686 | — | — | — | — | — |
| DFT [22] | Quadrupole | PAW [86] | 2850 | — | — | — | — | — |
| DFT [31] | Quadrupole | PAW [86] | 2400 | — | — | — | — | — |
| DFT [32] | Quadrupole | USPP [85] | 1970 | — | — | — | — | — |
| DFT [33] | Quadrupole | USPP [85] | 1800 | — | — | — | — | — |
| Exp [102] | | | 960 | — | — | — | — | — |

F-S potential [71] was reported in Ref. [75] and the value obtained is comparable to the one we obtain here with SNAP.

Our results show that for all four refractory metals, the Peierls stresses for edge dislocations on the $\{110\}$ and $\{123\}$ planes are relatively low compared to those on the $\{112\}$ plane. The highest Peierls stress is for W in the $\{112\}$ plane with 2276 MPa in the forward direction. In addition, no metal consistently achieves the highest or lowest Peierls stress for all planes. For example, among the four metals, Mo achieves the highest Peierls stress on the $\{110\}$ plane and W the highest on the $\{112\}$ and $\{123\}$ planes. The Peierls stresses are the lowest for Ta on the $\{123\}$ plane, and for W on the $\{110\}$ plane.

4.2.2. Peierls stress or CRSS of screw dislocations

Tables 7–10 present the Peierls stresses for screw dislocations in the four metals calculated here and by simulation or measured in experiments from other studies. Since screw character dislocations can cross slip, the screw dislocation may not necessarily glide on its habit plane when the deformation is applied. This behavior has been studied in detail in Ref. [89] and was attributed to the incorrect dislocation core structures rendered by the interatomic potentials. Here, in some metals and glide planes, we find that the dislocation glides on its habit plane, while in others it cross slips onto another plane. When it remains on its habit plane, the critical stress to move the dislocation is the Peierls stress. However, should it cross slip and glide on another plane, we refer to this motion as unstable and the critical stress for first motion as a critical resolved shear stress (CRSS) instead of a Peierls stress. In Tables 7–10, all CRSSes are marked with *. In a few studies, the critical

stresses were not reported when the screw dislocation cross slipped off-plane [60]. In other works, the critical stress was reported regardless of whether the dislocation actually moved on the intended plane; in these cases, the critical stress is referred to as the Peierls stress. Since the Peierls stress on the $\{110\}$ plane is expected to be symmetric, most prior studies did not specify the direction for which the Peierls stress is computed. Although their true directions are unknown, all Peierls stress calculated on the $\{110\}$ plane previously are listed as forward direction in Table 5.

In Table 7, for Mo, the SNAP Peierls stresses are higher in the $\{110\}$ and $\{112\}$ glide planes compared to those using other interatomic potentials, from experiments, and from DFT. For the $\{110\}$ plane, DFT calculations and experiments reported values in the range of 1350–2420 MPa, while previous MS and TB results ranged from 866–6192 MPa. Our result is 4054 MPa. This value is on average 1.54 times larger than those from non-ML interatomic potentials. It is more than twice the value obtained by Li et al. [73] using SNAP. As mentioned earlier, differences may arise from differences in the model size and model configuration used (PAD here vs. FBC there). We adopt a size that is two times large; it is known that the Peierls stress values are sensitive to simulation cell size [68].

For Nb, the Peierls stress on the $\{110\}$ plane by SNAP (840 MPa) is very close to those from DFT reported in the literature (650–860 MPa) [31,33] and is much lower than the CRSS predicted by an EAM potential (1313 MPa) [90]. In the SNAP calculation, the screw dislocation glides stably on the $\{110\}$ plane, whereas in the EAM calculation it does not. However, the opposite is true for the $\{112\}$ plane, where the screw

Table 11

Peierls stress or CRSS (in MPa) of a screw dislocation on the {112} plane in Ta and W based on different model configurations.

| Metal | Direction | PAD | FBC | FBS | Dipole-H | Dipole-V | Quadrupole |
|-------|---------------|-------|------|------|----------|----------|------------|
| Ta | Twinning | 893* | 973* | 990* | 948* | 925* | 936* |
| | Anti-twinning | 3583* | 3700 | 3643 | 3481* | 3582 | 3618 |
| W | Twinning | 3958* | 4046 | 4029 | 4081* | 4002* | 3991 |
| | Anti-twinning | 5937 | 6050 | 5980 | 5918 | 5975 | 5975 |

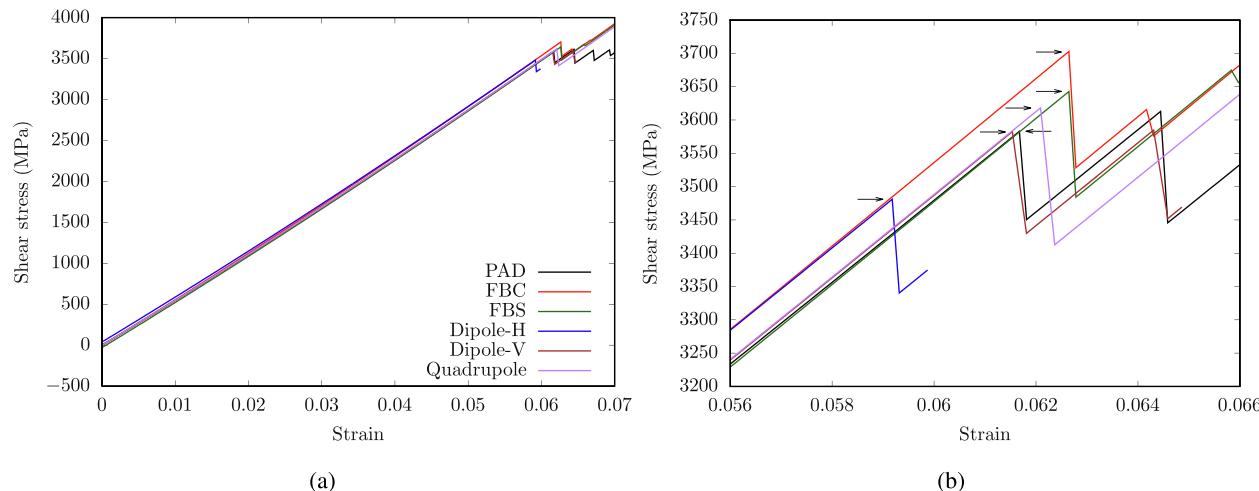


Fig. 4. Stress–strain curves for different models to calculate the Peierls stress or CRSS along the anti-twinning direction on the {112} plane in Ta. (b) is the zoom-in of a small region in (a) that encompasses the first stress drops, denoted by six arrows. Peierls stresses or CRSS are values of the shear stress at the first drop, which are summarized in the second row in Table 11.

dislocation cross slips away from the {112} plane in Nb by SNAP, whereas it glides stably by the two EAM potentials [90,55]. No DFT results on the {112} plane exist for Nb.

In Table 9, prior atomistic simulations for the {110} plane in Ta obtained Peierls stresses ranging from 655–5916 MPa and DFT results yielding 810–1760 MPa. Our SNAP-based CRSS value is 956 MPa, which is much closer to those based on DFT than those predicted by non-ML interatomic potentials.

In W, on the {110} plane, our SNAP-based Peierls stress is 3773 MPa, while DFT data range from 1800 to 2850 MPa. To the best of our knowledge, no non-ML potential has been applied to calculate the Peierls stress in W, for either an edge or screw dislocation, on any of the three planes studied here. Among the four metals, the SNAP-based Peierls stresses agree well with DFT measurements except for Mo and W. However, a prominent characteristic of ML potentials is its ability to improve through a proper expansion of training data. The current SNAP training data do not include any geometries containing dislocations. In theory, adding some geometries with dislocations explicitly included can improve the accuracy in Peierls stress measurements. It is also worth mentioning that these additional training data come with a higher computational cost.

Experimentally measured Peierls stresses in BCC metals are provided in the last rows of Tables 7–10. For Peierls stress calculations, screw dislocations on the {110} plane is the most commonly studied dislocation in the literature. For the {112} plane, no experimental results for screw dislocations have been previously reported. Calculations of Peierls stresses are quantitatively and consistently off from measurement. Measurements are typically much lower than any of the calculated Peierls stresses and they are even lower than the DFT data in all four

Table 12

CoV in Peierls stress or CRSS across all planes for each dislocation in each BCC metal. Results are based on MS simulations in this paper using SNAP, as presented in Tables 6–10.

| | Mo | Nb | Ta | W |
|-------|-------|-------|-------|-------|
| Edge | 0.839 | 1.025 | 1.25 | 1.116 |
| Screw | 0.125 | 0.437 | 0.646 | 0.186 |

metals. On the one hand, it can be concluded that atomistic calculations using interatomic potentials can be useful in providing trends and relative values of dislocation resistance, but not precise values. But on the other hand, it has been suggested that the low Peierls stresses for screw dislocations from experiments could be misleading due to possible internal stress concentrations that reduced the energy barrier for kink nucleation [74,103,104].

4.2.3. Effect of model configuration for screw dislocations

As mentioned, a recent work studied the effects of the model configuration on the Peierls stress values of an edge dislocation on the {112} plane in Nb [68]. Screw dislocations, however, were not studied there, and since edge dislocations glide stably on the habit plane, the question remains whether the model configuration can also affect the stability of screw dislocation glide.

To address this question, we examine the effect of model configuration on the glide of {112} screw dislocations in Ta and W. We consider five additional models apart from PAD: FBC, FBS, dipole-H, dipole-V, and quadrupole. Results presented in Table 11 find that the model configuration has a strong effect on the plane on which the screw

Table 13

Backward-to-forward ratios in the Peierls stresses or CRSS on three slip planes in four BCC metals. Results are based on MS simulations in this paper using SNAP, as presented in Tables 6–10.

| Metal | Dislocation | {110} | {112} | {123} |
|-------|-------------|-------|-------|-------|
| Mo | Edge | 0.971 | 0.685 | 0.9 |
| | Screw | 1 | 1.276 | 1.223 |
| Nb | Edge | 1.087 | 1.121 | 2.742 |
| | Screw | 0.985 | 1.45 | 0.483 |
| Ta | Edge | 1.05 | 1.062 | 1 |
| | Screw | 1 | 4.012 | 2.512 |
| W | Edge | 0.875 | 0.458 | 0.289 |
| | Screw | 1 | 1.5 | 1.239 |

dislocation ultimately glides. In Ta, the twinning direction glide is unstable in all models. The anti-twinning glide is also unstable when using the PAD and dipole-H model configurations, but stable when the other four model configurations are used. Notably, the stress-strain curves are all similar, as shown in Fig. 4, regardless of whether the glide is stable or not. In W, anti-twinning direction glide on the {112} plane is stable for all model configurations. The twinning direction, however, is unstable in the PAD, dipole-H, and dipole-V configurations, but stable in the other three. For the same metal, the Peierls stress values obtained under stable glide from the different configurations are close, lying within 1.8%, while the CRSS values obtained when the dislocation cross slips to another plane deviates slightly more, by 5.4%. Model configurations that support stable glide can yield consistent values, provided that all else is equal.

4.2.4. Anisotropy in critical stress

The degree of slip-plane anisotropy can be measured by calculating the coefficient of variation (CoV) in Peierls stresses or CRSS among all distinct planes belonging to each metal [60]. For each dislocation, the CoV is calculated as the standard deviation divided by the mean among the six cases (three slip planes, for each of which there are two shearing directions). The CoVs of the four metals are summarized in Table 12. For the edge dislocation, the four metals exhibit a similar degree of slip-plane anisotropy in the Peierls stress. These values are close to those from a recent MS study for four slip planes, additionally including the {113} plane, using EAM potentials: 1.13 for Mo and 1.31 for Nb [60]. On the other hand, screw dislocations possess smaller CoVs in Peierls stress or CRSS than edge dislocations, indicating that their critical stress values

are more uniform across different slip planes. For both dislocations, CoV is the highest in Ta and the lowest in Mo.

Another measure of stress anisotropy is glide asymmetry, the difference between the Peierls stress or CRSS in the forward and backward slip directions. Table 13 summarizes the glide asymmetry ratios. About the glide direction (i.e., x axis), the atomic structure of the {110} plane is symmetric (see Fig. 3(a,d)), and based on this geometric argument alone, the Peierls stress or CRSS is expected to be equal in the forward and backward direction. The calculated Peierls stresses or CRSS in the {110} plane exhibit near glide symmetry, with ratios ranging from 0.875–1.05. Despite this, in some cases, the motion of the screw dislocation is not necessarily symmetric. In Nb, for instance, the dislocation cross slips onto another plane when sheared in one direction but glides on the habit plane in the other.

For the {112} plane, glide asymmetry is expected for screw dislocations. Our results indicate glide asymmetry in all cases. For the screw dislocations, the Peierls stress or CRSS in the anti-twinning (AT) direction is always higher than that in the twinning (T) direction on all slip planes in all four metals, where the AT/T ratios range around 1.28–4.01. These ratios are similar to the range 1.170–4.85 from MS and 1.83–5.12 from DFT calculations (see Tables 7–10). The AT/T asymmetry on the {112} plane is also a good indicator of the non-Schmid effect, which is commonly observed in BCC metals [32]. This effect is captured by SNAP, as shown in Fig. 5. For edge dislocations, the glide asymmetry is not consistent as it is for screw dislocations. SNAP predicts that the anti-twinning Peierls stress is higher than the twinning one in Nb and Ta, but reversed in Mo and W. Evaluation of computed Peierls stress for edge dislocations from other studies also finds that the AT/T asymmetry depends on the material, interatomic potential, and model configuration [68,60].

Table 14

Screw-to-edge ratios in the Peierls stress or CRSS on different slip planes in four BCC metals. Results are based on MS simulations in this paper using SNAP, as presented in Tables 6–10.

| Metal | {110} _{fw} | {110} _{bw} | {112} _{fw} (T) | {112} _{bw} (AT) | {123} _{fw} | {123} _{bw} |
|-------|---------------------|---------------------|----------------------------|-----------------------------|---------------------|---------------------|
| Mo | 29.38 | 30.25 | 4.16 | 7.76 | 17.02 | 23.12 |
| Nb | 36.52 | 33.08 | 5.15 | 6.66 | 37.97 | 6.68 |
| Ta | 47.8 | 40.52 | 5.51 | 20.83 | 211.25 | 530.75 |
| W | 471.63 | 538.85 | 1.74 | 5.7 | 5.01 | 21.45 |

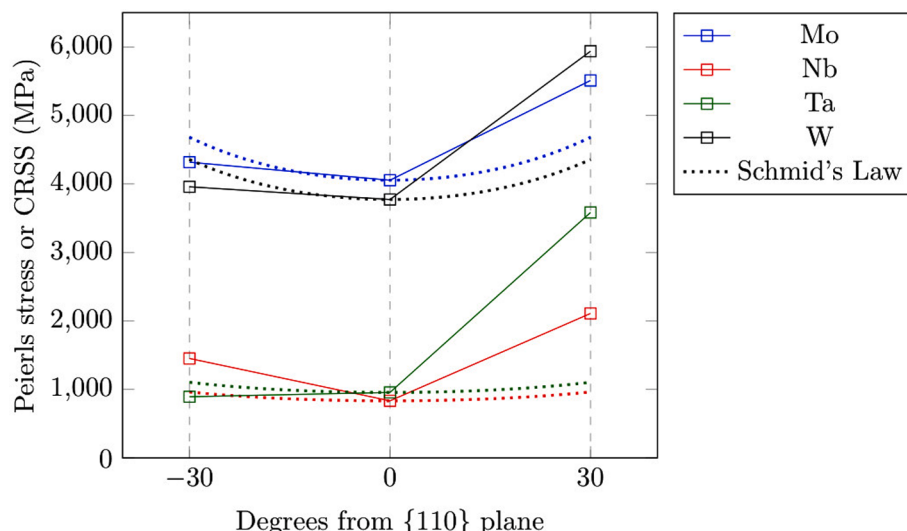


Fig. 5. Selected SNAP-based Peierls stresses or CRSS of screw dislocations in four BCC metals. Results for the {110} plane are averaged between forward and backward directions, which are denoted as $\bar{\sigma}_{110}$. Results based on Schmid's law follow $\bar{\sigma}_{110}/\cos\chi$, where χ is the degree from {110} plane. The anti-twinning and twinning directions on the {112} plane are, respectively, 30 and –30 degrees from the {110} plane.

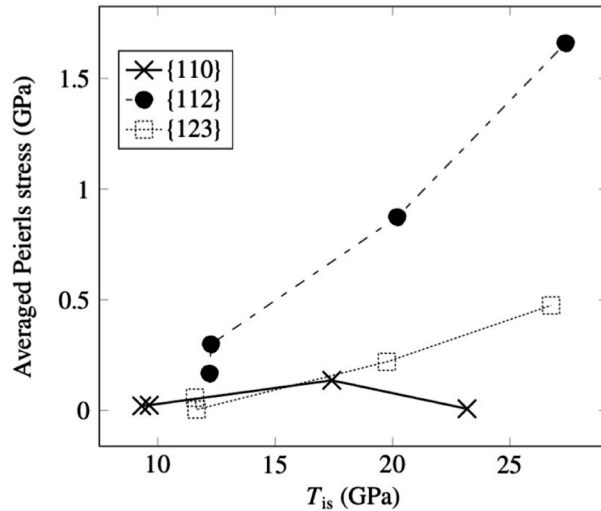
Table 15

Averaged Peierls stresses or CRSS (in MPa) on three slip planes in four BCC metals. Results are based on MS simulations in this paper using SNAP, as presented in Tables 6–10.

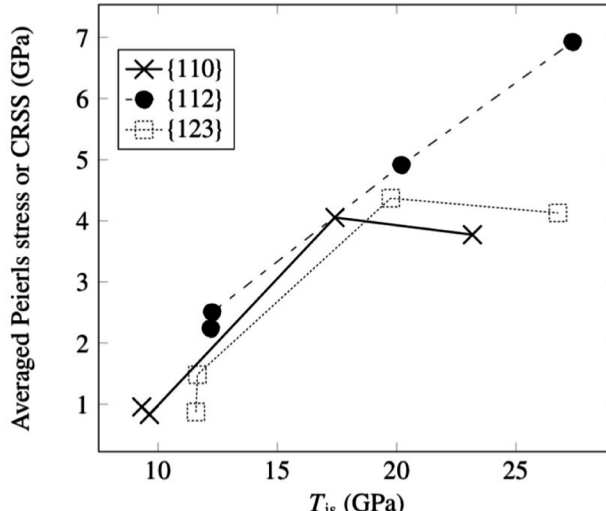
| Metal | Dislocation | {110} | {112} | {123} |
|-------|-------------|--------|--------|-------|
| Mo | Edge | 136 | 873.5 | 219.5 |
| | Screw | 4054 | 4913.5 | 4370 |
| Nb | Edge | 24 | 299 | 58 |
| | Screw | 833.5 | 1779 | 872.5 |
| Ta | Edge | 20.5 | 167 | 4 |
| | Screw | 956 | 2238 | 1484 |
| W | Edge | 7.5 | 1659 | 474.5 |
| | Screw | 3772.5 | 4947.5 | 4129 |

Like the {112} plane, the {123} plane exhibits similar glide asymmetry, where the ratio of Peierls stresses or CRSS in the two opposing senses of slip is 0.29–2.74. Unlike the {112} plane, however, the {123} plane has no association with twinning. For all metals except Nb, the forward slip direction on the {123} plane has a lower Peierls stress or CRSS than that in the backward direction.

The last measure of the anisotropy in critical stresses is the screw-to-edge ratio in the Peierls stress or CRSS along the same shear direction on the same slip plane. It is conventionally known that plasticity of BCC metals at low temperatures is controlled by the glide of screw dislocations since the Peierls stress and Peierls barrier are one to two orders of magnitude higher for screw dislocations than for edge dislocations [105,106]. In agreement, Peierls stresses for edge dislocations

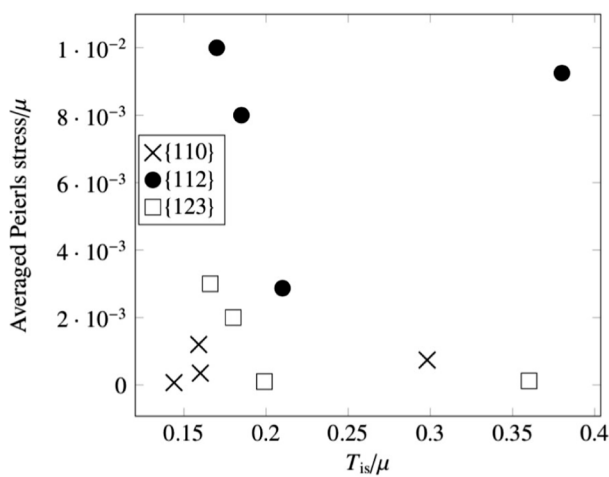


(a) Edge

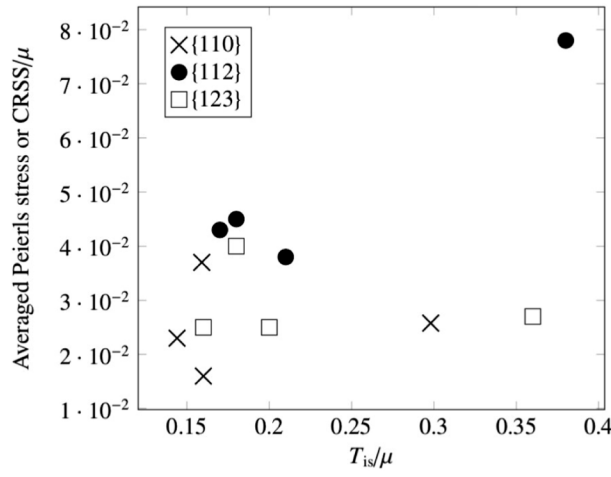


(b) Screw

Fig. 6. Averaged Peierls stress or CRSS vs. ideal shear strength T_{is} for (a) edge and (b) screw dislocations across different slip planes in the four metals. The lines drawn between symbols are intended to only guide the eye.



(a) Edge



(b) Screw

Fig. 7. Normalized averaged Peierls stress or CRSS/μ vs. normalized ideal shear strength T_{is}/μ for (a) edge and (b) screw dislocations across different slip planes in the four metals, where μ is the isotropic shear modulus in Hill form presented in Table 2.

calculated here are much smaller than those of screw dislocations. Screw-to-edge ratios in the Peierls stress or CRSS on different slip planes in four BCC metals are summarized in Table 14. It is shown that the ratios are generally high on the {110} plane, with the highest one being 538.85 for the backward direction in W. In some other cases, such as in the higher order {112} and {123} planes in Mo and W, the screw-to-edge ratios in the critical stress are remarkably much smaller, being in the range of 1.74–23.12. For W on the {112} plane, for instance, the ratio is only 1.74. Clearly with such low ratios, the effects of edge dislocation glide on plasticity cannot be considered negligible on these slip planes. As mentioned in Section 4.2.1, there is currently no *ab initio* or experimental data for the Peierls stresses of edge dislocations in either of the four BCC metals, so the screw-to-edge ratios based on *ab initio* calculations or experiments cannot be provided.

4.2.5. Correlation between ideal shear strength and Peierls stress

As mentioned in Section 1, there are two measures of glide resistance that can be obtained from atomistic simulations, the Peierls stress of a dislocation and the ideal shear strength T_{is} (Eq. 2). For the same plane, the averaged Peierls stress or CRSS between the forward and backward directions are calculated and presented in Table 15. Fig. 6 presents the averaged Peierls stress or CRSS versus T_{is} , indicating a generally positive correlation. The Peierls stress or CRSS on the higher order {112} and {123} planes are higher than that on the {110} plane in the same metal, just as the higher order planes possess higher T_{is} than the {110} plane. Experimental studies obtained similar ranking among the screw dislocations for the {110} plane. Specifically, the Peierls stresses for Mo and W are higher than those for Nb and Ta, with 730–870 MPa for Mo [87,88] and 960 MPa for W [102], as opposed to 415 MPa for Nb [91] and 340 MPa [101] for Ta. However, when the critical stresses are normalized by their corresponding shear modulus, no correlation is observed, see Fig. 7. This effect of normalization means that metals with high Peierls stresses or CRSS and T_{is} have a proportionally much higher shear modulus than metals with smaller critical stresses. From a physical viewpoint, the uncorrelatedness may not be surprising since Peierls stresses in BCC metals are known to not only depend on bonding across the plane but also on the atomic structure of the dislocation core [107,108], which is missing in the GSFE calculation.

5. Conclusions

In this work, the GSFE curves and Peierls stress or CRSS in four BCC refractory metals (Mo, Nb, Ta, W) are calculated using a recently developed ML-based interatomic potential called SNAP. The calculations focus on both screw and edge character dislocations on three common glide planes {110}, {112}, and {123}. On all three planes, the GSFE curves from SNAP agree well with those from DFT and when compared to non-ML interatomic potentials, are more accurate in calculations of the ideal shear strength. The SNAP-calculated GSFE curves on the higher order planes show lower degrees of asymmetry than the DFT curves. This can be regarded as an improvement from those calculated by other interatomic potentials, which produce symmetric curves for these planes. The fact that SNAP and other interatomic potentials give rise to less or no asymmetry suggests that asymmetry can only be exhibited when quantum effects are well captured.

We show that SNAP provides screw dislocation Peierls stresses close to those of DFT, much closer than those achieved by non-ML potentials. Like DFT, the values are still higher than those from the few experimentally measured values in the literature. For all metals, the edge dislocation Peierls stress are the lowest on the {110} plane and the highest on the {112} plane. For screw dislocations, glide on either the {110} or {123} plane is the easiest. Both the {112} and {123} planes

exhibit glide asymmetry, being on average 1.9 times higher in one direction than the other. The screw-to-edge ratio is large, in the range of ≈ 29–539 for the {110} plane, but substantially smaller, in the range of ≈ 2–21, for the {112} plane. The slip-plane anisotropy, the difference in the Peierls stresses or CRSS among the three distinct crystallographic planes, is the greatest for Ta and minimal for Mo, for both edge and screw dislocations. Last, we observed that in most cases, the screw dislocation cross slips away from the habit plane, and this outcome can change depending on the model configuration used, i.e., PAD, FBC, FBS, dipole-H, dipole-V, or quadrupole. Besides static properties such as GSFEs and Peierls stresses, dynamic dislocation properties are also important [109]. Specifically for BCC metals, kink activation enthalpy and kink-controlled dislocation mobility are critical. Those calculations however would involve much longer dislocation lines. For example, a recent MD work studied kink dynamics along screw dislocations in Fe and W using EAM potentials [110], with the dislocation line length being 30–450 nm. In comparison, the current work used a much shorter dislocation line, < 2.2 nm. As mentioned, the computational cost of SNAP is generally two to three orders of magnitude higher than that of EAM. Therefore, application of SNAP to kink dynamics would require high computational effort.

6. Data availability

The data that support the findings of this study are available from Mr. Xiaowang Wang (email: xiaowangwang@ucsb.edu) upon reasonable request.

CRediT authorship contribution statement

Xiaowang Wang: Validation, Formal analysis, Investigation, Writing - original draft, Writing - review & editing, Visualization. **Shuozi Xu:** Conceptualization, Methodology, Validation, Investigation, Writing - original draft, Writing - review & editing, Project administration, Visualization. **Wu-Rong Jian:** Conceptualization, Methodology. **Xiang-Guo Li:** Data curation, Methodology. **Yanqing Su:** Data curation, Visualization. **Irene J. Beyerlein:** Supervision, Funding acquisition, Writing - original draft, Writing - review & editing.

Declaration of Competing Interest

The authors declare that they have no known competing financial interests or personal relationships that could have appeared to influence the work reported in this paper.

Acknowledgements

XW would like to thank Yuanchao Hu for helpful discussions on using LAMMPS. WJ and IJB would like to acknowledge funding from the Office of Naval Research under Grant No. N000141712810. SX and IJB gratefully acknowledge support from the Office of Naval Research under contract ONR BRC Grant N00014-18-1-2392. Use was made of computational facilities purchased with funds from the National Science Foundation (CNS1725797) and administered by the Center for Scientific Computing (CSC). The CSC is supported by the CNSI and the Materials Research Science and Engineering Center (MRSEC; NSF DMR 1720256) at UC Santa Barbara.

Appendix A. Bulk energy per atom vs pre-defined lattice parameter

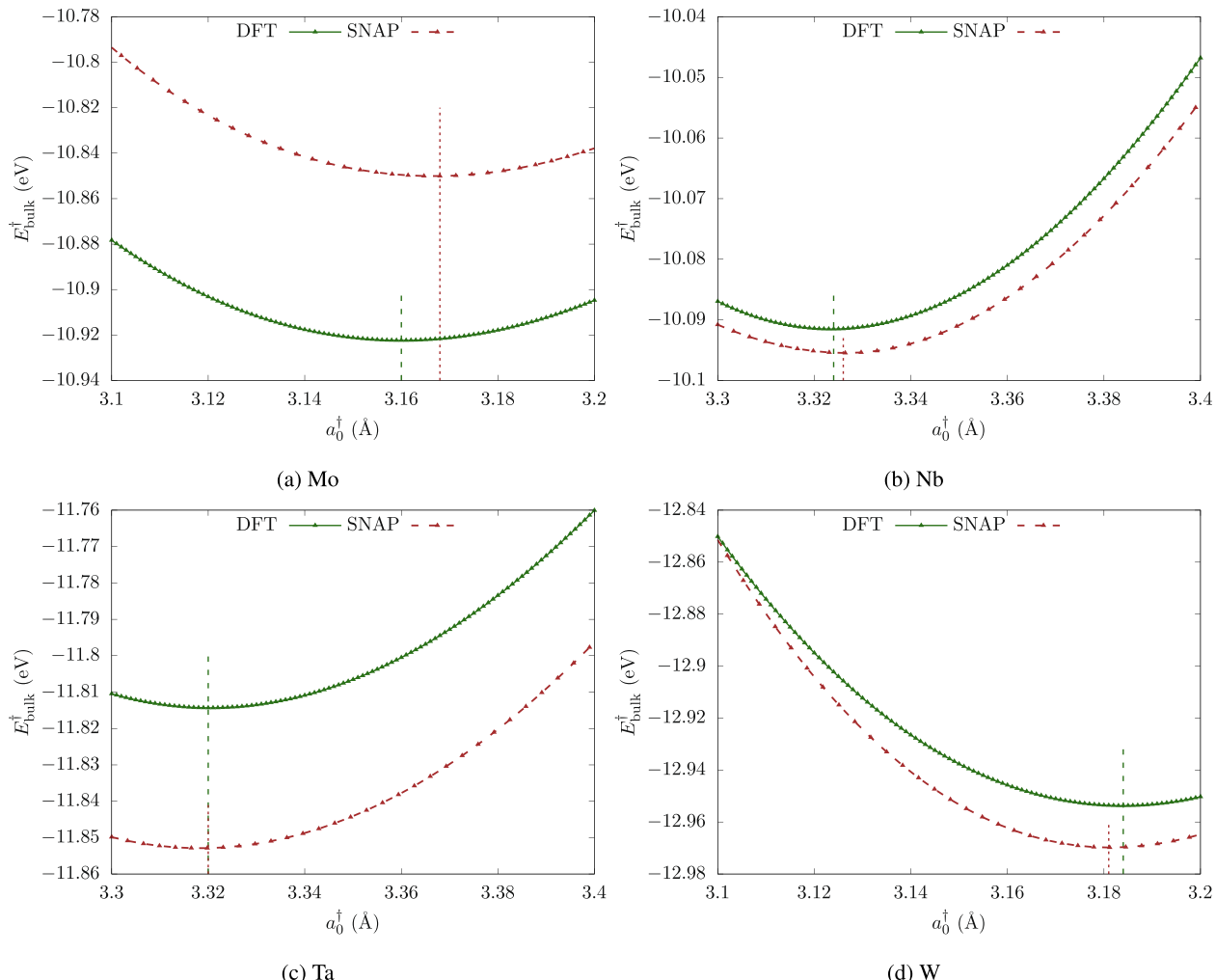


Fig. A.1. Bulk energy per atom $E_{\text{bulk}}^{\dagger}$ vs pre-defined lattice parameter a_0^{\dagger} in four BCC metals based on SNAP. DFT results are from Ref. [16]. Dashed vertical lines indicate the lowest point on each curve.

Appendix B. Relaxing atoms along the x direction in GSFE calculations

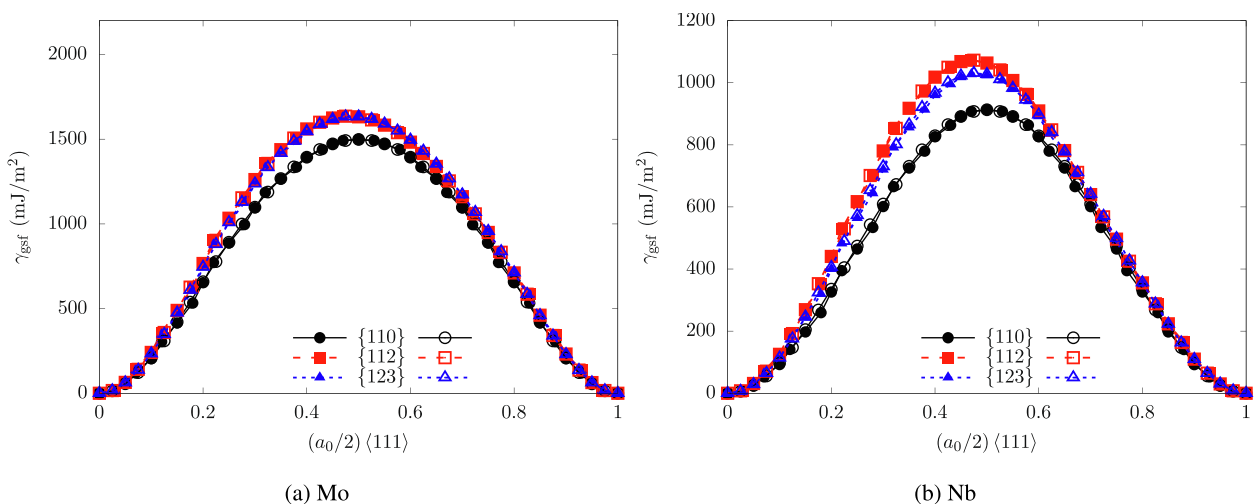


Fig. B.2. GSFE curves on the three planes in Mo and Nb based on SNAP. Filled symbols denote relaxation of atoms along both x and y directions while open symbols denote relaxation of atoms along the y direction only.

Appendix C. Effects of atomic plane numbers in GSFE calculations

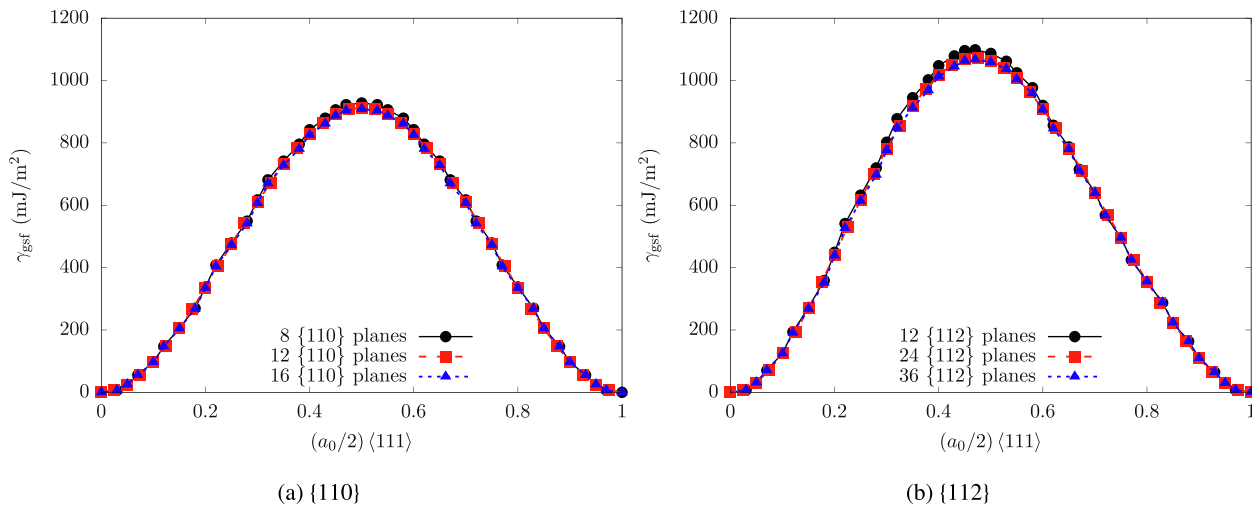


Fig. C.3. Relaxed GSFE curves on two slip planes in Nb based on SNAP. Different numbers of atomic plane along the slip plane normal are considered.

Appendix D. Effects of number of GSFE values along one curve

Table D.1

Values of USFs γ_{usf} (in mJ/m²) and ideal shear strengths T_{is} (in GPa) calculated based on GSFE curves containing 41 and 101 values, respectively.

| Plane | | No. of GSFE values | Ta | W |
|-------|-----------------------|--------------------|--------|--------|
| {110} | γ_{usf} | 41 | 830.8 | 1910.3 |
| | | 101 | 830.8 | 1910.3 |
| | T_{is} | 41 | 9.32 | 23.17 |
| | | 101 | 9.37 | 23.32 |
| {112} | γ_{usf} | 41 | 977.64 | 2121 |
| | | 101 | 977.64 | 2121.1 |
| | T_{is} | 41 | 12.21 | 27.37 |
| | | 101 | 12.29 | 27.51 |
| {123} | γ_{usf} | 41 | 950.93 | 2114.2 |
| | | 101 | 951.88 | 2114.5 |
| | T_{is} | 41 | 11.65 | 26.75 |
| | | 101 | 11.695 | 26.91 |

References

- [1] T.E. Tietz, J.W. Wilson, *Behavior and Properties of Refractory Metals*, Stanford University Press, 1965.
- [2] S. Xu, Modelling plastic deformation of nano/submicron-sized tungsten pillars under compression: A coarse-grained atomistic approach, *Int. J. Multiscale Comput. Eng.* 16 (4) (2018) 367–376, ISSN 1543-1649, 1940-4352, 10.1615/IntJMultCompEng.2018026027, URL: <http://www.dl.begellhouse.com/journals/61fd1b191cf7e96f,77bb56c9113fd8ad,519a0e1634b8eddd.html>.
- [3] T. Trusty, S. Xu, I.J. Beyerlein, Atomistic simulations of tungsten nanotubes under uniform tensile loading, *J. Appl. Phys.* 126 (9) (2019) 095105, ISSN 0021-8979, 10.1063/1.5110167, URL: <https://aip.scitation.org/doi/full/10.1063/1.5110167>.
- [4] F. Wang, G.H. Balbus, S. Xu, Y. Su, J. Shin, P.F. Rottmann, K.E. Knippling, J.-C. Stinville, L.H. Mills, O.N. Senkov, I.J. Beyerlein, T.M. Pollock, D.S. Gianola, Multiplicity of dislocation pathways in a refractory multiprincipal element alloy, *Science* 370 (6512) (2020) 95–101, ISSN 0036-8075, 1095-9203, 10.1126/science.aba3722, URL: <https://science.sciencemag.org/content/370/6512/95>.
- [5] K. Maier, M. Peo, B. Saile, H. Schaefer, A. Seeger, High-temperature positron annihilation and vacancy formation in refractory metals, *Philos. Mag. A* 40 (5) (1979) 701–728.
- [6] V.S. Prasad, R. Baligidad, A.A. Gokhale, *Niobium and other high temperature refractory metals for aerospace applications*, in: *Aerospace Materials and Material Technologies*, Springer, 2017, pp. 267–288.
- [7] D. Inman, S.H. White, The production of refractory metals by the electrolysis of molten salts; design factors and limitations, *J. Appl. Electrochem.* 8 (5) (1978) 375–390, ISSN 1572-8838, DOI: 10.1007/BF00615833, URL: doi: 10.1007/BF00615833.
- [8] S. Xu, S.Z. Chavoshi, Y. Su, Deformation mechanisms in nanotwinned tungsten nanopillars: Effects of coherent twin boundary spacing, *Phys. Stat. Solidi RRL* 12 (3) (2018a) 1700399, ISSN 1862-6270, 10.1002/pssr.201700399, URL: <https://onlinelibrary.wiley.com/doi/abs/10.1002/pssr.201700399>.
- [9] D. Hull, D.J. Bacon, *Introduction to Dislocations*, Butterworth-Heinemann, fifth ed., ISBN 0080966721, 2011.
- [10] R. Attree, J. Plaskett, *XCI: The self-energy and interaction energy of stacking faults in metals*, *Philos. Mag.* 1 (10) (1956) 885–911.
- [11] A. Kumar, B. Kedjar, Y. Su, L. Thilly, I.J. Beyerlein, Atomic-level calculations and experimental study of dislocations in InSb, *J. Appl. Phys.* 127 (13) (2020) 135104, ISSN 0021-8979, 10.1063/1.5139285, URL: <https://aip.scitation.org/doi/10.1063/1.5139285>.
- [12] R. Peierls, The size of a dislocation, *Proc. Phys. Soc.* 52 (1) (1940) 34–37, <https://doi.org/10.1088/0959-5309/52/1/305>.
- [13] B. Joós, M. Duesbery, The Peierls stress of dislocations: an analytic formula, *Phys. Rev. Lett.* 78 (2) (1997) 266.
- [14] S.H. Haghighat, J. von Pezold, C. Race, F. Körmann, M. Friák, J. Neugebauer, D. Raabe, Influence of the dislocation core on the glide of the 1/2⟨111⟩{1 1 0} edge dislocation in bcc-iron: An embedded atom method study, *Comput. Mater. Sci.* 87 (2014) 274–282.
- [15] J. Christian, Some surprising features of the plastic deformation of body-centered cubic metals and alloys, *Metall. Trans. A* 14 (7) (1983) 1237–1256.
- [16] S. Xu, Y. Su, L.T.W. Smith, I.J. Beyerlein, Frank-Read source operation in six body-centered cubic refractory metals, *J. Mech. Phys. Solids* 141 (2020) 104017, ISSN 0022-5096, 10.1016/j.jmps.2020.104017, URL: <http://www.sciencedirect.com/science/article/pii/S0022509620302520>.
- [17] S.L. Frederiksen, K.W. Jacobsen, Density functional theory studies of screw dislocation core structures in bcc metals, *Philos. Mag.* 83 (3) (2003) 365–375, ISSN 1478-6435, DOI: 10.1080/0141861021000034568, URL: doi: 10.1080/0141861021000034568.
- [18] R.F. Zhang, J. Wang, I.J. Beyerlein, T.C. Germann, Twinning in bcc metals under shock loading: a challenge to empirical potentials, *Philos. Mag. Lett.* 91 (12) (2011) 731–740, ISSN 0950-0839, DOI: 10.1080/09500839.2011.615348, URL: doi: 10.1080/09500839.2011.615348.
- [19] C. Yang, L. Qi, Modified embedded-atom method potential of niobium for studies on mechanical properties, *Comput. Mater. Sci.* 161 (2019) 351–363, ISSN 0927-0256, 10.1016/j.commatsci.2019.01.047, URL: <http://www.sciencedirect.com/science/article/pii/S0927025619300473>.
- [20] L. Yang, P. Söderlind, J.A. Moriarty, Accurate atomistic simulation of (a/2)111 screw dislocations and other defects in bcc tantalum, *Philos. Mag. A* 81 (5) (2001) 1355–1385.
- [21] X. Zhang, J. Tang, L. Deng, G. Zhong, X. Liu, Y. Li, H. Deng, W. Hu, The effects of interstitial impurities on the mechanical properties of vanadium alloys: A first-principles study, *J. Alloys Compd.* 701 (2017) 975–980, ISSN 0925-8388, 10.1016/j.jallcom.2017.01.135, URL: <http://www.sciencedirect.com/science/article/pii/S0925838817301597>.

- [22] L. Romaner, C. Ambrosch-Draxl, R. Pippan, Effect of rhenium on the dislocation core structure in tungsten, *Phys. Rev. Lett.* 104 (19) (2010), 195503, <https://doi.org/10.1103/PhysRevLett.104.195503>. URL: <https://link.aps.org/doi/10.1103/PhysRevLett.104.195503>.
- [23] M.-C. Marinica, L. Ventelon, M.R. Gilbert, L. Proville, S.L. Dudarev, J. Marian, G. Bencteux, F. Willaime, Interatomic potentials for modelling radiation defects and dislocations in tungsten, *J. Phys.: Condens. Matter* 25 (39) (2013) 395502, ISSN 0953-8984, 10.1088/0953-8984/25/39/395502, URL: <http://stacks.iop.org/0953-8984/25/i=39/a=395502>.
- [24] G. Bonny, D. Terentyev, A. Bakaev, P. Grigorev, D.V. Neck, Many-body central force potentials for tungsten, *Modelling Simul. Mater. Sci. Eng.* 22 (5) (2014) 053001, ISSN 0965-0393, 10.1088/0965-0393/22/5/053001, URL: <http://stacks.iop.org/0965-0393/22/i=5/a=053001>.
- [25] S. Xu, J.K. Startt, T.G. Payne, C.S. Deo, D.L. McDowell, Size-dependent plastic deformation of twinned nanopillars in body-centered cubic tungsten, *J. Appl. Phys.* 121 (17) (2017) 175101, ISSN 0021-8979, 10.1063/1.4982754, URL: <http://aip.scitation.org/doi/10.1063/1.4982754>.
- [26] J. Qian, C.Y. Wu, J.L. Fan, H.R. Gong, Effect of alloying elements on stacking fault energy and ductility of tungsten, *J. Alloys Compd.* 737 (2018) 372–376, ISSN 0925-8388, 10.1016/j.jallcom.2017.12.042, URL: <http://www.sciencedirect.com/science/article/pii/S0925838817342172>.
- [27] B. Bienvenu, C.C. Fu, E. Clouet, Impact of magnetism on screw dislocations in body-centered cubic chromium, *Acta Mater.* 200 (2020) 570–580, ISSN 1359-6454, 10.1016/j.actamat.2020.09.041, URL: <http://www.sciencedirect.com/science/article/pii/S1359645420307357>.
- [28] C. Woodward, S. Rao, Ab-initio simulation of isolated screw dislocations in bcc Mo and Ta, *Philos. Mag. A* 81 (5) (2001) 1305–1316.
- [29] C. Woodward, S. Rao, Flexible ab initio boundary conditions: Simulating isolated dislocations in bcc Mo and Ta, *Phys. Rev. Lett.* 88 (21) (2002), 216402.
- [30] F. Shimizu, S. Ogata, H. Kimizuka, T. Kano, J. Li, H. Kaburaki, First-principles calculation on screw dislocation core properties in bcc molybdenum, *J. Earth Sim.* 7 (2007) 17–21.
- [31] C.R. Weinberger, G.J. Tucker, S.M. Foiles, Peierls potential of screw dislocations in bcc transition metals: Predictions from density functional theory, *Phys. Rev. B: Condens. Matter* 87 (5) (2013), 054114.
- [32] L. Dezerald, D. Rodney, E. Clouet, L. Ventelon, F. Willaime, Plastic anisotropy and dislocation trajectory in BCC metals, *Nat. Commun.* 7 (2016) 11695.
- [33] L. Dezerald, L. Ventelon, E. Clouet, C. Denoual, D. Rodney, F. Willaime, Ab initio modeling of the two-dimensional energy landscape of screw dislocations in bcc transition metals, *Phys. Rev. B* 89 (2) (2014), 024104, <https://doi.org/10.1103/PhysRevB.89.024104>. URL: <https://link.aps.org/doi/10.1103/PhysRevB.89.024104>.
- [34] D. Segall, A. Strachan, W.A. Goddard III, S. Ismail-Beigi, T. Arias, Ab initio and finite-temperature molecular dynamics studies of lattice resistance in tantalum, *Phys. Rev. B: Condens. Matter* 68 (1) (2003), 014104.
- [35] S.Z. Chavoshi, S. Xu, Nanoindentation/scratching at finite temperatures: Insights from atomistic-based modeling, *Prog. Mater. Sci.* 100 (2019) 1–20, ISSN 0079-6425, DOI: 10.1016/j.pmatsci.2018.09.002, URL: <http://www.sciencedirect.com/science/article/pii/S0079642518300914>.
- [36] S. Xu, Y. Su, D. Chen, L. Li, An atomistic study of the deformation behavior of tungsten nanowires, *Appl. Phys. A* 123 (12) (2017) 788, ISSN 0947-8396, 1432-0630, DOI: 10.1007/s00339-017-1414-3, URL: <https://link.springer.com/article/10.1007/s00339-017-1414-3>.
- [37] S. Xu, Y. Su, S.Z. Chavoshi, Deformation of periodic nanovoid structures in Mg single crystals, *Mater. Res. Express* 5 (1) (2018) 016523, ISSN 2053-1591, 10.1088/2053-1591/aaa678, URL: <http://stacks.iop.org/2053-1591/5/i=1/a=016523>.
- [38] S. Xu, Y. Su, Dislocation nucleation from symmetric tilt grain boundaries in body-centered cubic vanadium, *Phys. Lett. A* 382 (17) (2018) 1185–1189, ISSN 0375-9601, DOI: 10.1016/j.physleta.2018.03.002, URL: <http://www.sciencedirect.com/science/article/pii/S0375960118302287>.
- [39] L. Proville, D. Rodney, M.-C. Marinica, Quantum effect on thermally activated glide of dislocations, *Nature Mater.* 11 (10) (2012) 845–849, ISSN 1476-1122, DOI: 10.1038/nmat3401, URL: <http://www.nature.com/nmat/journal/v11/n10/full/nmat3401.html>.
- [40] D. Dragoni, T.D. Daff, G. Csányi, N. Marzari, Achieving DFT accuracy with a machine-learning interatomic potential: Thermomechanics and defects in bcc ferromagnetic iron, *Phys. Rev. Mater.* 2 (1) (2018), 013808.
- [41] P. Rowe, G. Csányi, D. Alfe, A. Michaelides, Development of a machine learning potential for graphene, *Phys. Rev. B: Condens. Matter* 97 (5) (2018), 054303.
- [42] V. Quaranta, J. Behler, M. Hellström, Structure and dynamics of the liquid–water/zinc-oxide interface from machine learning potential simulations, *J. Phys. Chem.* 123 (2) (2018) 1293–1304.
- [43] V.L. Deringer, G. Csányi, Machine learning based interatomic potential for amorphous carbon, *Phys. Rev. B: Condens. Matter* 95 (9) (2017), 094203.
- [44] Y. Su, S. Xu, I.J. Beyerlein, Ab initio-informed phase-field modeling of dislocation core structures in equal-molar CoNiRu multi-principal element alloys, *Modelling Simul. Mater. Sci. Eng.* 27 (8) (2019) 084001, ISSN 0965-0393, 10.1088/1361-651X/ab3b62, URL: <https://doi.org/10.1088/2F1361-651x%2Fab3b62>.
- [45] J. Byggmästar, K. Nordlund, F. Djurabekova, Gaussian approximation potentials for body-centered-cubic transition metals, *Phys. Rev. Mater.* 4 (9) (2020), 093802, <https://doi.org/10.1103/PhysRevMaterials.4.093802>. URL: <https://link.aps.org/doi/10.1103/PhysRevMaterials.4.093802>.
- [46] Y. Zuo, C. Chen, X. Li, Z. Deng, Y. Chen, J. Behler, G. Csányi, A.V. Shapeev, A.P. Thompson, M.A. Wood, et al., Performance and cost assessment of machine learning interatomic potentials, *J. Phys. Chem. A* 124 (4) (2020) 731–745.
- [47] C. Chen, Z. Deng, R. Tran, H. Tang, I.-H. Chu, S.P. Ong, Accurate force field for molybdenum by machine learning large materials data, *Phys. Rev. Mater.* 1 (4) (2017), 043603.
- [48] X.-G. Li, C. Hu, C. Chen, Z. Deng, J. Luo, S.P. Ong, Quantum-accurate spectral neighbor analysis potential models for Ni-Mo binary alloys and fcc metals, *Phys. Rev. B: Condens. Matter* 98 (9) (2018), 094104.
- [49] A.P. Thompson, L.P. Swiler, C.R. Trott, S.M. Foiles, G.J. Tucker, Spectral neighbor analysis method for automated generation of quantum-accurate interatomic potentials, *J. Comput. Phys.* 285 (2015) 316–330.
- [50] Y. Su, M. Ardeljan, M. Knezevic, M. Jain, S. Pathak, I.J. Beyerlein, Elastic constants of pure body-centered cubic Mg in nanolaminates, *Comput. Mater. Sci.* 174 (2020) 109501, ISSN 0927-0256, 10.1016/j.commatsci.2019.109501, URL: <http://www.sciencedirect.com/science/article/pii/S0927025619308006>.
- [51] S. Xu, E. Hwang, W.-R. Jian, Y. Su, I.J. Beyerlein, Atomistic calculations of the generalized stacking fault energies in two refractory multi-principal element alloys, *Intermetallics* 124 (2020), 106844.
- [52] S. Plimpton, Fast parallel algorithms for short-range molecular dynamics, *J. Comput. Phys.* 117 (1) (1995) 1–19.
- [53] Y. Su, S. Xu, I.J. Beyerlein, Density functional theory calculations of generalized stacking fault energy surfaces for eight face-centered cubic transition metals, *J. Appl. Phys.* 126 (10) (2019) 105112, ISSN 0021-8979, 10.1063/1.5115282, URL: <https://aip.scitation.org/doi/10.1063/1.5115282>.
- [54] X.W. Zhou, R.A. Johnson, H.N.G. Wadley, Misfit-energy-increasing dislocations in vapor-deposited CoFe/NiFe multilayers, *Phys. Rev. B* 69 (2004), 144113, <https://doi.org/10.1103/PhysRevB.69.144113>. URL: <https://link.aps.org/doi/10.1103/PhysRevB.69.144113>.
- [55] D.-Y. Lin, S.S. Wang, D.L. Peng, M. Li, X.D. Hui, An n-body potential for a Zr-Nb system based on the embedded-atom method, *J. Phys.: Condens. Matter* 25 (10) (2013) 105404, ISSN 0953-8984, 10.1088/0953-8984/25/10/105404, URL: <https://doi.org/10.1088/0953-8984/2F25%2F10%2F105404>.
- [56] Y. Su, S. Xu, On the role of initial void geometry in plastic deformation of metallic thin films: A molecular dynamics study, *Mater. Sci. Eng.: A* 678 (2016) 153–164, ISSN 0921-5093.
- [57] S. Xu, Y. Su, D. Chen, L. Li, Plastic deformation of Cu single crystals containing an elliptic cylindrical void, *Mater. Lett.* 193 (2017) 283–287, ISSN 0167-577X.
- [58] J. Xu, S. Xu, I.J. Beyerlein, Atomistic simulations of dipole tilt wall stability in thin films, *Thin Solid Films* 689 (2019) 137457, ISSN 0040-6090.
- [59] D. Chen, S. Xu, Y. Kulkarni, Atomistic mechanism for vacancy-enhanced grain boundary migration, *Phys. Rev. Mater.* 4 (3) (2020), 033602, <https://doi.org/10.1103/PhysRevMaterials.4.033602>. URL: <https://link.aps.org/doi/10.1103/PhysRevMaterials.4.033602>.
- [60] S. Xu, Y. Su, W.-R. Jian, I.J. Beyerlein, Local slip resistances in equal-molar MnNbTi multi-principal element alloy, *Acta Mater.* 202 (2021) 68–79, ISSN 1359-6454, 10.1016/j.actamat.2020.10.042, URL: <http://www.sciencedirect.com/science/article/pii/S1359645420308405>.
- [61] Y.N. Osetsky, D.J. Bacon, An atomic-level model for studying the dynamics of edge dislocations in metals, *Model. Simul. Mater. Sci. Eng.* 11 (4) (2003) 427.
- [62] S. Xu, J.R. Mianroodi, A. Hunter, I.J. Beyerlein, B. Svendsen, Phase-field-based calculations of the disregistry fields of static extended dislocations in FCC metals, *Phil. Mag.* 99 (11) (2019) 1400–1428, ISSN 1478-6435.
- [63] S. Xu, L. Smith, J.R. Mianroodi, A. Hunter, B. Svendsen, I.J. Beyerlein, A comparison of different continuum approaches in modeling mixed-type dislocations in Al, *Modelling Simul. Mater. Sci. Eng.* 27 (7) (2019) 074004, ISSN 0965-0393.
- [64] S. Xu, Y. Su, I.J. Beyerlein, Modeling dislocations with arbitrary character angle in face-centered cubic transition metals using the phase-field dislocation dynamics method with full anisotropic elasticity, *Mech. Mater.* 139 (2019) 103200, ISSN 0167-6636.
- [65] W.-R. Jian, M. Zhang, S. Xu, I.J. Beyerlein, Atomistic simulations of dynamics of an edge dislocation and its interaction with a void in copper: a comparative study, *Modelling Simul. Mater. Sci. Eng.* 28 (4) (2020) 045004, ISSN 0965-0393, 10.1088/1361-651X/ab8358, URL: <https://doi.org/10.1088/1361-651X/ab8358>.
- [66] A. Stukowski, Visualization and analysis of atomistic simulation data with OVITO—the Open Visualization Tool, *Modell. Simul. Mater. Sci. Eng.* 18 (1) (2009), 015012.
- [67] A. Stukowski, Structure identification methods for atomistic simulations of crystalline materials, *Modelling Simul. Mater. Sci. Eng.* 20 (4) (2012) 045021, ISSN 0965-0393, 10.1088/0965-0393/20/4/045021, URL: <https://doi.org/10.1088/0965-0393/20/4/045021>.
- [68] W.-R. Jian, S. Xu, I.J. Beyerlein, On the significance of model design in atomistic calculations of the Peierls stress in Nb, *Comput. Mater. Sci.* 188 (2021) 110150, ISSN 0927-0256, 10.1016/j.commatsci.2020.110150, URL: <http://www.sciencedirect.com/science/article/pii/S0927025620306418>.
- [69] E. Bitzek, P. Koskinen, F. Gähler, M. Moseler, P. Gumbsch, Structural relaxation made simple, *Phys. Rev. Lett.* 97 (17) (2006), 170201.
- [70] M. Duesbery, V. Vitek, Plastic anisotropy in b.c.c. transition metals, *Acta Mater.* 46 (5) (1998) 1481–1492.
- [71] G. Ackland, R. Thetford, An improved N-body semi-empirical model for body-centred cubic transition metals, *Philos. Mag. A* 56 (1) (1987) 15–30.
- [72] K.-I. Masuda, A. Sato, Electronic theory for screw dislocation in BCC transition metals: Calculation of the peierls stress and the core energy, *Philos. Mag. B* 37 (4) (1978) 531–536.
- [73] X.-G. Li, C. Chen, H. Zheng, Y. Zuo, S.P. Ong, Complex strengthening mechanisms in the NbMoTaW multi-principal element alloy, *npj Comput. Mater.* 6 (2020) 70.
- [74] H. Park, M.R. Fellinger, T.J. Lenosky, W.W. Tipton, D.R. Trinkle, S.P. Rudin, C. Woodward, J.W. Wilkins, R.G. Hennig, Ab initio based empirical potential used

- to study the mechanical properties of molybdenum, *Phys. Rev. B: Condens. Matter* 85 (21) (2012), 214121.
- [75] K. Kang, V.V. Bulatov, W. Cai, Singular orientations and faceted motion of dislocations in body-centered cubic crystals, *Proc. Natl. Acad. Sci. U.S.A.* 109 (38) (2012) 15174–15178.
- [76] J. Li, C.-Z. Wang, J.-P. Chang, W. Cai, V.V. Bulatov, K.-M. Ho, S. Yip, Core energy and Peierls stress of a screw dislocation in bcc molybdenum: A periodic-cell tight-binding study, *Phys. Rev. B: Condens. Matter* 70 (10) (2004), 104113.
- [77] M. Mrovec, D. Nguyen-Manh, D.G. Pettifor, V. Vitek, Bond-order potential for molybdenum: Application to dislocation behavior, *Phys. Rev. B: Condens. Matter* 69 (9) (2004), 094115.
- [78] J.A. Moriarty, V. Vitek, V.V. Bulatov, S. Yip, Atomistic simulations of dislocations and defects, *J. Comput.-Aided Mater. Des.* 9 (2) (2002) 99–132, ISSN 1573–4900, DOI: 10.1023/A:1026022602578, URL: doi: 10.1023/A:1026022602578.
- [79] S. Rao, C. Woodward, Atomistic simulations of $(a/2)$ 111 screw dislocations in bcc Mo using a modified generalized pseudopotential theory potential, *Philos. Mag. A* 81 (5) (2001) 1317–1327.
- [80] J.A. Moriarty, Analytic representation of multi-ion interatomic potentials in transition metals, *Phys. Rev. B* 42 (1990) 1609–1628, <https://doi.org/10.1103/PhysRevB.42.1609>. URL: https://link.aps.org/doi/10.1103/PhysRevB.42.1609.
- [81] W. Xu, J.A. Moriarty, Accurate atomistic simulations of the Peierls barrier and kink-pair formation energy for 111 screw dislocations in bcc Mo, *Comput. Mater. Sci.* 9 (3–4) (1998) 348–356.
- [82] J.A. Moriarty, W. Xu, P. Söderlind, J. Belak, L.H. Yang, J. Zhu, Atomistic simulations for multiscale modeling in bcc metals, *J. Eng. Mater. Tech.* 121 (2) (1999) 120–125, ISSN 0094–4289, DOI: 10.1115/1.2812355, URL: https://asmedigitalcollection.asme.org/materialstechnology/article/121/2/120/40376/Atomistic-Simulations-for-Multiscale-Modeling-in.
- [83] K. Ito, V. Vitek, Atomistic study of non-Schmid effects in the plastic yielding of bcc metals, *Philos. Mag. A* 81 (5) (2001) 1387–1407.
- [84] H. Haas, C.Z. Wang, M. Fähnle, C. Elsässer, K.M. Ho, Environment-dependent tight-binding model for molybdenum, *Phys. Rev. B* 57 (1998) 1461–1470, <https://doi.org/10.1103/PhysRevB.57.1461>. URL: https://link.aps.org/doi/10.1103/PhysRevB.57.1461.
- [85] D. Vanderbilt, Soft self-consistent pseudopotentials in a generalized eigenvalue formalism, *Phys. Rev. B* 41 (11) (1990) 7892–7895, <https://doi.org/10.1103/PhysRevB.41.7892>. URL: https://link.aps.org/doi/10.1103/PhysRevB.41.7892.
- [86] G. Kresse, D. Joubert, From ultrasoft pseudopotentials to the projector augmented-wave method, *Phys. Rev. B: Condens. Matter* 59 (3) (1999) 1758.
- [87] L. Hollang, D. Brunner, A. Seeger, Work hardening and flow stress of ultrapure molybdenum single crystals, *Mater. Sci. Eng., A* 319 (2001) 233–236.
- [88] Y. Aono, E. Kuramoto, K. Kitajima, Fundamental plastic behaviors in high-purity BCC metals (Nb, Mo and Fe), in: Strength of Metals and Alloys (ICSMA 6), Elsevier, 9–14, 1982.
- [89] L.M. Hale, J.A. Zimmerman, C.R. Weinberger, Simulations of bcc tantalum screw dislocations: Why classical inter-atomic potentials predict 112 slip, *Comput. Mater. Sci.* 90 (2014) 106–115.
- [90] M.R. Fellingher, H. Park, J.W. Wilkins, Force-matched embedded-atom method potential for niobium, *Phys. Rev. B* 81 (14) (2010), 144119.
- [91] S. Takeuchi, T. Hashimoto, K. Maeda, Plastic deformation of bcc metal single crystals at very low temperatures, *Trans. Jpn. Inst. Met.* 23 (2) (1982) 60–69.
- [92] D. Segall, T. Arias, A. Strachan, W. Goddard, Accurate calculations of the Peierls stress in small periodic cells, *J. Comput.-Aided Mater. Des.* 8 (2–3) (2001) 161–172.
- [93] A. Strachan, T. Çağın, O. Güleren, S. Mukherjee, R.E. Cohen, W.A. Goddard III, First principles force field for metallic tantalum, *Modelling Simul. Mater. Sci. Eng.* 12 (4) (2004) S445–S459, ISSN 0965–0393, DOI: 10.1088/0965-0393/12/4/S10, URL: <https://doi.org/10.1088/0965-0393/12/4/S10>.
- [94] A. Guellil, J. Adams, The application of the analytic embedded atom method to bcc metals and alloys, *J. Mater. Res.* 7 (3) (1992) 639–652.
- [95] Y. Li, D.J. Siegel, J.B. Adams, X.-Y. Liu, Embedded-atom-method tantalum potential developed by the force-matching method, *Phys. Rev. B* 67 (2003), 125101, <https://doi.org/10.1103/PhysRevB.67.125101>. URL: <https://link.aps.org/doi/10.1103/PhysRevB.67.125101>.
- [96] X. Zhou, H. Wadeley, R.A. Johnson, D. Larson, N. Tabat, A. Cerezo, A. Petford-Long, G. Smith, P. Clifton, R. Martens, et al., Atomic scale structure of sputtered metal multilayers, *Acta Mater.* 49 (19) (2001) 4005–4015.
- [97] Y. Mishin, A. Lozovoi, Angular-dependent interatomic potential for tantalum, *Acta Mater.* 54 (19) (2006) 5013–5026.
- [98] G. Wang, A. Strachan, T. Cagin, W.A. Goddard III, Molecular dynamics simulations of $1/2$ a_{111} screw dislocation in Ta, *Mater. Sci. Eng., A* 309 (2001) 133–137.
- [99] G. Wang, A. Strachan, T. Çağın, W.A. Goddard III, Calculating the Peierls energy and Peierls stress from atomistic simulations of screw dislocation dynamics: application to bcc tantalum, *Modell. Simul. Mater. Sci. Eng.* 12 (4) (2004) S371.
- [100] C. Woodward, S. Kajihara, L.H. Yang, Site preferences and formation energies of substitutional Si, Nb, Mo, Ta, and W solid solutions in $\text{Li}_{10}\text{Ti-Al}$, *Phys. Rev. B* 57 (21) (1998) 13459–13470, <https://doi.org/10.1103/PhysRevB.57.13459>. URL: <https://link.aps.org/doi/10.1103/PhysRevB.57.13459>.
- [101] S. Takeuchi, K. Maeda, Slip in high purity tantalum between 0.7 and 40 K, *Acta Metall.* 25 (12) (1977) 1485–1490.
- [102] D. Brunner, J. Diehl, V. Glebovsky, The plastic behavior of high-purity tungsten, in: in: Proceedings of the 5th International Conference on Ultra High-Purity Materials, 1998, pp. 83–92.
- [103] R. Gröger, V. Vitek, Explanation of the discrepancy between the measured and atomistically calculated yield stresses in body-centred cubic metals, *Philos. Mag. Lett.* 87 (2) (2007) 113–120.
- [104] T. Suzuki, H. Koizumi, Inertial motion and multi-kink pair formation of dislocations on the Peierls potential, *Philos. Mag. A* 67 (5) (1993) 1153–1160.
- [105] D. Caillard, Kinetics of dislocations in pure Fe. Part I. In situ straining experiments at room temperature, *Acta Mater.* 58 (9) (2010) 3493–3503.
- [106] D. Caillard, Kinetics of dislocations in pure Fe. Part II. In situ straining experiments at low temperature, *Acta Mater.* 58 (9) (2010b) 3504–3515, ISSN 1359–6454, doi: 10.1016/j.actamat.2010.02.024, URL: <http://www.sciencedirect.com/science/article/pii/S1359645410001102>.
- [107] S.Z. Xu, Z.M. Hao, Y.Q. Su, Y. Yu, Q. Wan, W.J. Hu, An analysis on nanovoid growth in body-centered cubic single crystalline vanadium, *Comput. Mater. Sci.* 50 (8) (2011) 2411–2421, ISSN 0927–0256, DOI: 10.1016/j.commatsci.2011.03.019, URL: <http://www.sciencedirect.com/science/article/pii/S0927025611001625>.
- [108] S. Xu, Y. Su, Nanovoid growth in BCC α -Fe: influences of initial void geometry, *Model. Simul. Mater. Sci. Eng.* 24 (8) (2016) 085015, ISSN 0965–0393, 10.1088/0965-0393/24/8/085015, URL: <http://stacks.iop.org/0965-0393/24/i=8/a=085015>.
- [109] L. Xiong, J. Rigelesaiyin, X. Chen, S. Xu, D.L. McDowell, Y. Chen, Coarse-grained elastodynamics of fast moving dislocations, *Acta Mater.* 104 (2016) 143–155, ISSN 1359–6454, 10.1016/j.actamat.2015.11.037, URL: <http://www.sciencedirect.com/science/article/pii/S1359645415300884>.
- [110] R. Ji, T. Phan, H. Chen, L. Xiong, Quantifying the dynamics of dislocation kinks in iron and tungsten through atomistic simulations, *Int. J. Plast.* 128 (2020), 102675.